The dynamic response of floating offshore wind turbine platform in wave–current condition

View Online   Export Citation   CrossMark

Xiang Li (李翔),[1] (iD) Qing Xiao (肖清),[1,a] (iD) Enhao Wang (王恩浩),[2] (iD) Christophe Peyrard,[3] (iD)
and Rodolfo T. Gonçalves[4] (iD)

AFFILIATIONS

[1]Department of Naval Architecture, Ocean and Marine Engineering, University of Strathclyde, Glasgow, United Kingdom
[2]Tsinghua Shenzhen International Graduate School, Shenzhen, China
[3]Saint-Venant Hydraulics Laboratory (Électricité de France, ENPC), Université Paris, Chatou, France
[4]OSPL - Ocean Space Planning Laboratory, Department of Systems Innovation, School of Engineering, The University of Tokyo, Tokyo, Japan

Note: This paper is part of the special topic, Recent Advances in Marine Hydrodynamics.
[a]Author to whom correspondence should be addressed: qing.xiao@strath.ac.uk

ABSTRACT

In this paper, the fluid–structure interaction of floating offshore wind turbine (FOWT) platforms under complex ocean conditions is investigated using OpenFOAM and in-house developed models. Two types of FOWT platform, i.e., a semi-submersible platform and a barge platform, are studied for their dynamic responses to either wave or current. The results reveal that a semi-submersible platform exhibits larger cross-flow motion and lock-in phenomenon, while a barge platform experiences smaller motion with no significant lock-in within the velocity range examined. The combined wave–current conditions are further studied for the semi-submersible platform, with different angles between wave and current, the current speeds, and wave parameters. Unlike other investigations focusing on colinear wave–current interaction, in which the waves usually mitigate vortex-induced motion (VIM); here, we find that waves might lead to an enhanced VIM with a large angle between current and wave. The evaluation on the interaction effect factor shows that the largest wave height in the lock-in region does not lead to the most dangerous scenario, herein, the largest platform motion. Instead, a smaller wave height with a large wave period can induce even larger motion.

I. INTRODUCTION

The increasing demand for renewable energy has led to the growth of wind energy, with floating offshore wind turbines (FOWTs) being a promising solution for generating energy in deep water where traditional turbines are unable to operate. FOWTs also benefit from greater and more consistent wind resources in deeper water and eliminate the visual impact associated with near-shore turbines.[1,2] Several FOWT designs, such as OC4 DeepCwind,[3] Hywind,[4] and TetraSpar,[5] have been developed extensively. For FOWTs, their applications are expected to expand to more diverse locations, which may present more complex sea states, resulting in more significant challenges in ensuring adequate stability, power output, and reliability under diverse operating conditions, for the design of FOWT, and this has been investigated extensively both numerically and experimentally in our previous studies[6–8] and other researchers.[9–14]

In addition to wave–platform interaction, the appearance of water current in some areas of sea may lead to additional platform motion, known as vortex-induced motion (VIM). This phenomenon usually occurs when a cylindrical structure or a bluff body is moored or elastically mounted in the presence of current. The amplitude of the response can be particularly high when the frequency of vortex shedding becomes synchronized with the structure vibration frequency.[15,16] Such synchronization is known as lock-in, and it occurs over a wide range of flow velocity.

The VIM of cylinders and monocolumn platforms has been extensively studied experimentally.[17–19] It was found that the platform follows a classic eight-shaped orbital trajectory for some cases. This low-frequency response, especially in cross-flow (CF) direction, may result in potential damage to FOWT's mooring system and cause fatigue problem.[20] The in-line (IL) motion is relatively small compared to that in the CF direction.

Compared to wave, current–platform interaction gets less attention during the design process of FOWT platform. This is partially because the water current caused by wind has a characteristic speed of

0.05–0.5 m/s, which is less than the minimal threshold required for VIM to occur. The speed of tidal current is usually larger than surface current, whose maximum value can be as large as 4.5 m/s as observed in some channel areas,[21] with a water depth ranging from 40 to 110 m, but this velocity is much smaller in deep, open ocean. However, in certain locations, such as the Gulf Stream, the current velocity at the free surface can exceed 2 m/s, which is sufficiently large to induce VIM for a floating platform having cylinders, such as SPAR.[22–24] The semi-submersible (SS) platform, on the other hand, has a smaller aspect ratio (draft/characteristic length), which has been investigated by Gonçalves et al.[25,26] Their experimental findings confirmed that VIM occurs even at a relatively low current speed for two SS platforms with different geometric dimensions. Other research regarding VIM of different platforms can also be found recently.[27,28] Due to the inherent disadvantage of potential-flow theory method, in which fluid is assumed irrotational and non-viscous, numerical analysis involving offshore structure–fluid interaction has been conducted using the finite element method[29] (FEM) or computational fluid dynamics (CFD) method. The later considers viscosity of fluid directly by solving the Navier–Stokes equation with turbulence models.[30–34] In their studies, the formation and shedding of the vortices due to VIM is clearly observed.

A combined colinear wave–current interaction with four square columns platform is further studied experimentally.[35,36] The findings indicated that the adding of wave sometimes tends to have little impact on VIM, while mitigating VIM entirely in other cases. This is further observed in the studies of Maximiano et al.[37] and Li et al.[38] A detailed examination on the fluid flow vorticity field indicated that the reduced amplitude of VIM is caused by the wave interaction with current and platform, changing the vortex shedding pattern, and thus the vortex shedding frequency.

While VIM mitigation by waves is observed in past studies, most of existing investigations are focused on the flow condition where wave and current are aligned. In reality, it is very likely the angle between the wave and current can vary in different sea states. For instance, in the project of LIFE50+ for a 10 MW wind turbine, the wave and current inter-angle ranges from 82.5° to 150° at three deployment sites with a water depth over 50 m.[39] It is, therefore, critical to understand the wave–current–structure interaction under various angles and flow conditions.

In this paper, the dynamic response of the floating platform in complex sea conditions is numerically studied using a high-fidelity CFD tool.[40] We aim at illustrating the underlying mechanisms that are related to the wave–current interaction with FOWT platforms using this tool. The rest of the paper is organized as follows. The numerical method including the governing equations of the fluid dynamics, the structural dynamics, and the mooring system will first be presented in Sec. II, together with a description of the physical problem to be studied and the parameters for both the OC4 DeepCwind platform by National Renewable Energy Laboratory (NREL) and the BW IDEOL platform with Électricité de France. Section III displays the numerical results, where the wave-only, current-only conditions are first examined for two FOWT platforms as comparisons. Then, the combined wave–current condition studies for the OC4 platform at various wave–current angles and wave parameters are conducted, and the conclusions are drawn in the last section.

II. PROBLEM STATEMENT

The wave–current interaction of the FOWT platform is simulated using an integrated toolbox based on the OpenFOAM code. Particularly, the solver is a multiphase flow solver interFoam in OpenFOAM. To apply mooring lines as restraints, an in-house code is integrated into interFoam. Additionally, a wave generation boundary condition and active wave absorbing scheme are implemented in the simulation.[6]

A. Numerical method

For a fluid problem, the Reynolds number $Re = UL/\nu$ is one non-dimensional parameter to differentiate between laminar and turbulent flows, where U is the fluid velocity, L is the characteristic length of the structure, and ν is the kinematic viscosity. In this study, Re ranges from 8000 to 40 000 for current-only cases; thus, the turbulence model is needed. The vortex shedding and the flow field surrounding structure are essential components in understanding VIM. As such, it is crucial to capture a precise structure of the vortex, a task which is normally not optimally accomplished by utilizing the standard Reynolds-averaged Navier–Stokes (RANS) model due to its highly numerical dissipation. In this study, large eddy simulation (LES) wall-adapted local eddy-viscosity (WALE) model[41] is used. In LES, the largest, most energy-containing turbulent structures (large eddies) are explicitly resolved on the computational grid, while the smaller, more isotropic structures (small eddies or subgrid scales) are modeled. The unsteady, incompressible Naiver–Stokes equations are solved in the LES model,

$$\frac{\partial \overline{u_i}}{\partial x_i} = 0, \tag{1}$$

$$\frac{\partial \bar{u}_i}{\partial t} + (\bar{u}_j - u_g)\frac{\partial \bar{u}_i}{\partial x_j} = -\frac{1}{\rho}\frac{\partial \bar{p}}{\partial x_i} + \frac{\partial}{\partial x_j}\left[v\left(\frac{\partial \bar{u}_i}{\partial x_j} + \frac{\partial \bar{u}_j}{\partial x_i}\right) \right] - \frac{\partial \tau_{ij}}{\partial x_j} - g_i, \tag{2}$$

where u_i is the velocity component in the i-direction, $\overline{u}_i$ is the filtered velocity, and u_g is the speed of the motion of the mesh grid. ρ is the density, and p denotes the dynamic pressure. g is the gravity acceleration, and t is the time. N is the kinematic viscosity of the fluid, and τ_{ij} is the subgrid-scale stress as follows:

$$\tau_{ij} = \overline{u_i u_j} - \overline{u_i}\,\overline{u_j}. \tag{3}$$

In order to capture the fluid motion at the air–water free surface, the volume of fluid (VOF) method[42] is applied to solve the two-phase flow problem. The volume fraction (α) is governed by the following transport equation:

$$\frac{\partial \alpha}{\partial t} + \nabla \cdot ((u - u_g)\alpha) + \nabla \cdot (u_r(1 - \alpha)\alpha) = 0. \tag{4}$$

To better capture an accurate interface, it is crucial to maintain a sharp interface and ensure that the α remains conservative and bounded between 0 and 1. To achieve this, OpenFOAM utilizes an artificial compression term $\nabla \cdot [u_r(1 - \alpha)\alpha]$, where u_r is a velocity field used to compress the interface and only functions near the free surface. For a water–air problem, fluid density and viscosity can be written as a mixture of water and air,

$$\rho = \alpha \rho_w + (1 - \alpha) \rho_\alpha, \tag{5}$$

$$\mu = \alpha \mu_w + (1 - \alpha) \mu_\alpha, \tag{6}$$

where ρ_w and ρ_a denote the density of water and air, and μ_w and μ_a denote their dynamic viscosity.

To generate numerical waves, the fluid velocity at the inlet boundary is prescribed using the Stokes second-order wave theory,

$$u = \frac{\pi H}{T} \frac{\cosh k(z+d)}{\sinh kd} \cos \beta + \frac{3\pi H}{4T} \left(\frac{\pi H}{L}\right) \frac{\cosh 2k(z+d)}{\sinh^4 kd} \cos 2\beta, \tag{7}$$

$$w = \frac{\pi H}{T} \frac{\sinh k(z+d)}{\sinh kd} \sin \beta + \frac{3\pi H}{4T} \left(\frac{\pi H}{L}\right) \frac{\sinh 2k(z+d)}{\sinh^4 kd} \sin 2\beta, \tag{8}$$

where H and T denote the wave height and wave period, k and d denote the wave number and water depth, and β is the phase.

In this paper, to impose non-reflection boundary conditions on the computational outlet boundary, an active wave absorbing scheme is utilized, with which the waves are directly absorbed along the boundary without relaxation zones.[43] This can significantly reduce the computational domain size required by the relaxation zone.[6,44] The primary concept is to produce waves with a phase opposite to that of the incident waves, but with the same characteristics at the outlet boundary. The corrected velocity at the outlet boundary is described by

$$\Delta u = -\Delta \eta \frac{\pi H}{T} \frac{\cosh k(z+d)}{\sinh kd}, \tag{9}$$

where $\Delta \eta$ is the difference of the surface elevation η due to reflected waves. In this paper, two different models of moorings are utilized for two separate platforms. For the modeling of the spring-type mooring, it is simulated as a linear force proportional to the displacement,

$$f = k_s x, \tag{10}$$

where k_s is the stiffness of the spring, and x is the position of the center of rotation.

To model the catenary mooring lines constraining the platform, a quasi-static mooring line analysis model is utilized, in which a mooring line is treated as multiple segments with identical length.[45] For each segment, equations of static equilibrium are established in both horizontal and vertical directions, which can be illustrated in Fig. 1. The equilibrium equations are

$$T_{x(i+1)} = T_i, \quad T_{z(i+1)} = T_{iz} + w_i dl, \tag{11}$$

where T is the tension, and w_i is the unit weight of each segment. To consider the extension of the mooring lines, each segment should be subjected to the following geometric constraints:

$$ds \cos(\varphi_{i+1}) = x_i' + x_{i+1}' = \triangle x', \\ ds \sin(\varphi_{i+1}) = z_{i+1}' + z_i' = \triangle z', \tag{12}$$

$$ds = dl \left(1 + \frac{T_{i+1}}{EA}\right), \tag{13}$$

where ds is the stretch length of the segment, and E and A denote Young's modulus and cross-sectional area for the segment, respectively.
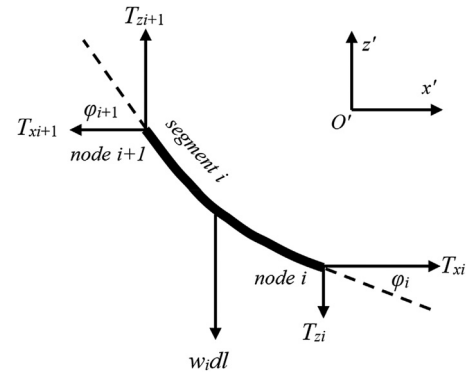

FIG. 1. Sketch of the segment in the mooring line analysis model.

Although the mooring lines are not directly simulated using CFD, the hydrodynamic forces are estimated by using Morison's equation. The fluid information is derived from the field information from the CFD background mesh at the corresponding positions. The dynamic response of the platform is governed by the following motion equations:

$$m\ddot{x} + c\dot{x} + kx = F_x, \tag{14a}$$

and

$$m\ddot{y} + c\dot{y} + ky = F_y, \tag{14b}$$

where m, c, and k represent the platform mass, structural damping coefficient, and spring stiffness, respectively. F_x and F_y denote the IL and CF hydrodynamic force acting on the platform. The Newmark-beta method is adopted to solve Eq. (13) for the motion of the platform. To ensure simulation stable, an acceleration relaxation factor of 0.9 is adopted. Since we focus on the IL and CF motion of the platform, only x and y degrees of freedom are considered.

B. Model description

The two platforms studied are OC4 semi-submersible platform and a barge IDEOL platform as shown in Fig. 2. The OC4 semi-submersible platform model is based on a 1:73 model test performed at the University of Tokyo by Gonçalves et al.[26] The platform is made up of four columns, one central column with a smaller diameter and three offset columns with larger diameters. Columns are connected by crossbars in between. There are base columns attached below the side columns. In the experiment, the model was restrained by four perpendicular mooring lines. The main parameters, including the equivalent stiffness of the mooring system, are summarized in Table I. The natural frequencies of the platform in IL and CF directions are 9.4 and 9.6 s, respectively, which were obtained via free decay tests.

The barge IDEOL platform is a 1:50 model, which was experimentally tested in the National Research Institute of Fisheries Engineering (NRIFE) wave tank in Japan,[46] shown in Fig. 2(b). The width of the barge semi-submersible platform is 0.82 m, with a draught of 0.14 m. The skirt with 0.055 m width is attached at the bottom to reduce the dynamics motion response. Compared to the OC4 platform, this barge platform has a simpler geometry and is easier to
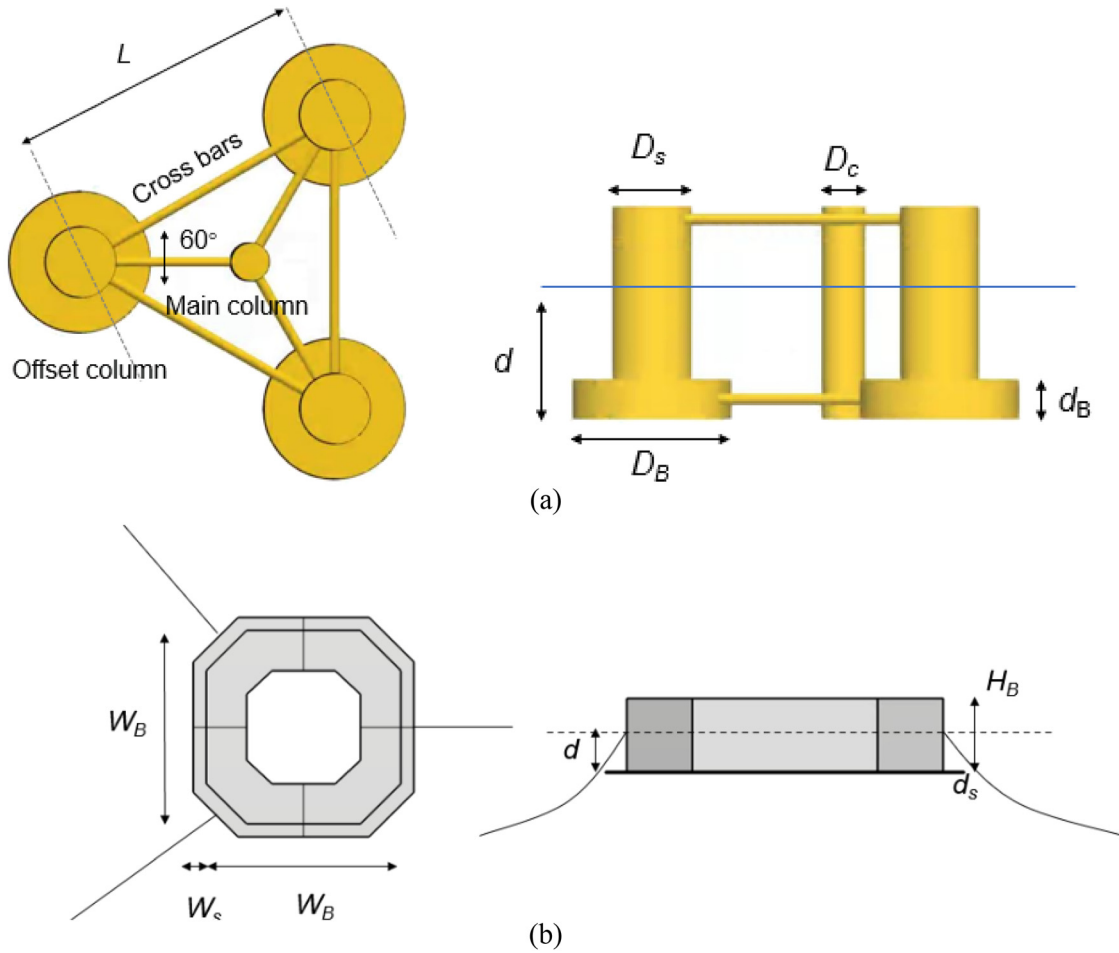
FIG. 2. Sketch of the scale-down model for (a) OC4 platform and (b) IDEOL platform.

TABLE I. Geometric parameters and the mooring parameters.

OC4 platform		IDEOL platform	
Central column diameter	$D_c = 0.09$ m	Thickness of skirt plate	$d_s = 0.004$ m
Offset Column diameter	$D_s = 0.165$ m	Skirt plate width	$W_S = 0.055$ m
Base column diameter	$D_B = 0.33$ m	Width	$W_B = 0.82$ m
Height of base column	$d_B = 0.083$ m	Height	$H_B = 0.19$ m
Platform draft	$d = 0.27$ m	Platform draft	$d = 0.14$ m
Distance between offset columns	$L = 0.688$ m		
Inertia properties			
Mass of the platform	$m = 36.7$ kg	Mass of the platform	$m = 62.31$ kg
Center of mass	$z_c = -0.134$ m	Center of mass	$z_c = 0.03$ m
Mooring parameters			
Stiffness in x direction	$k_x = 27.5$ N/m	Type	Studless
Stiffness in y direction	$k_y = 28.1$ N/m	Weight in water	0.067 kg/m

construct, with a larger area of water plane and smaller draft. To constrain the platform, three catenary mooring lines are applied. The nominal diameter of these studless chains is 3 mm with a total length of 8 m. The geometric parameters of the platform can be found in Fig. 2 and Table I.

In ocean engineering, the geometry of a platform significantly influences its motion response, particularly in interaction with water currents. The above-mentioned two platforms exhibit distinct geometries, primarily differentiated by their waterplane (WP) area. The IDEOL barge platform, akin to a hollowed-out box, has a substantially larger WP area compared to the SS platform. This expands WP area results in a shallower draft and a reduced aspect ratio (defined as draft/characteristic length). In a vortex-induced motion (VIM) study, a lower aspect ratio typically exhibits enhanced three-dimensional characteristics at the platform's bottom edge, subsequently altering the motion amplitude.

C. CFD settings

The computational domain is shown in Fig. 3 with top and side views. The boundary conditions are set as follows: The zero-gradient pressure condition is applied at the inlet and outlet boundaries with the air speed equal to zero, while the fluid velocity is given by a build-in boundary based on the wave theory, for the generation of inflow wave–current condition and wave absorbing. For those cases with oblique incident waves, the front boundary is imposed the same settings as the inlet boundary condition for wave generating. A non-slip wall boundary condition is applied to the bottom.
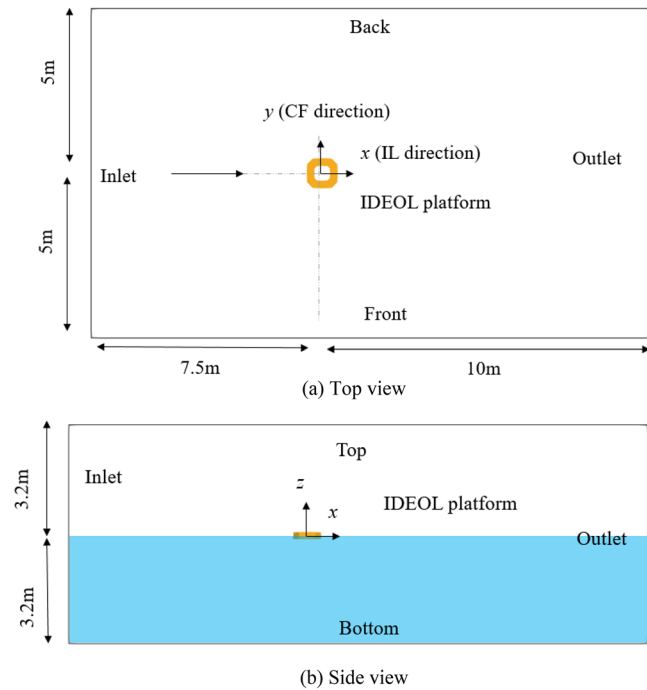

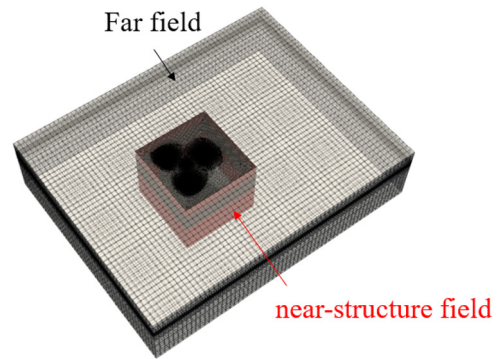FIG. 3. (a) Top view and (b) side view of the numerical wave tank for IDEOL platform.

FIG. 4. Computational mesh for the OC4 platform, and the inner red zone is structured mesh to capture boundary layers with high quality, outside which is the unstructured far-field mesh, where the mesh is only refined near the water–air surface.

To accurately model the motion of platform under both wave and current conditions, it is essential to ensure that the mesh resolution meets different mesh density requirements. For instance, to capture VIM, the separation of the boundary layer around the structure and the vortex street at the downstream should be accurately modeled. Therefore, CFD mesh is refined at the near wall field region as well as the wake region. To reduce the overall cell numbers of the computational domain, a hybrid mesh is used, which is made up of the near-field structured mesh (red one) and the far-field unstructured mesh as shown in Fig. 4. Within the boundary layer, the thickness of the mesh is set that the $y+$ around the platforms ranges from 1.0 to 4.0. The surface cell on the platform is 1/100 of the characteristic length D. At the near field of the structure, the average cell size is 1/50D. At the far field region, to ensure the accuracy of numerical wave generation, the cells near air–water free surface are refined. In particular, at least eight cells are used along the z direction per wave height and at least 180 cells per wavelength.

The convergence test of the numerical simulation is conducted, and the results are shown in Table II. Three mesh sets with different cell counts are used, with which the normalized IL and CF motions (A_x/D and A_y/D) are compared, as well as the frequency of the cross-flow oscillation f/f_n. The disparity between the medium and fine cases is less significant than that between the intermediate and coarse cases. This suggests that the intermediate grid is sufficient fine for the current research. Similarly, for the sensitivity study with different time steps, the predicted motion hardly changes when $U\Delta t/D < 0.002$.

TABLE II. Sensitivity study for computational mesh and unsteady time step for the OC4 platform with $V_r = 8.1$.

Mesh	Cell count	$U\Delta t/D$	A_x/D	A_y/D	f/f_n
Coarse	2650k	0.002	0.050	0.424	0.990
Intermediate	3510k	0.001	0.055	0.403	0.959
		0.002	0.059	0.410	0.958
		0.004	0.077	0.421	0.932
Fine	5400k	0.002	0.061	0.402	0.959

TABLE III. Wave and current parameters for the OC4 platform testing.

Wave parameters									
H (m) Scaled 1:73	0.02	0.04	0.07	0.09	0.116		T (s) Scaled 1:73	1.5	2.0	2.63
H (m) Full-scale	1.45	2.91	5.09	6.54	8.44		T (s) Full-scale	12.78	17.04	22.4
Current parameters									
U (m/s) Scaled 1:73		0.05	0.08	0.11	0.14	0.17	0.20	0.24
U (m/s) Full-scale		0.43	0.68	0.94	1.20	1.45	1.70	2.05
Vr		2.30	3.7	4.6	8.1	9.9	11.6	14.3

Considering the cost of computational time, a time step of $U\Delta t/D = 0.002$ is chosen for the CFD modeling in this study.

PIMPLE [a combination of Pressure Implicit with Splitting of Operator (PISO) and Semi-Implicit Method for Pressure-Linked Equations (SIMPLE)] algorithm is utilized to solve the pressure–velocity coupling. A second-order Crank–Nicolson scheme is used for temporal discretization. The second-order upwind scheme is adopted for convective terms. Gradient terms are handled via a second-order cell-limited Gauss linear scheme. The total cell of the simulation is around 350×10^6 for both platforms. The computations are made in parallel with five nodes (180 cores) for each case on Cirrus HPC (http://www.cirrus.ac.uk). The average simulation time is $3T_n$ per day, which may vary depending on the specific cases.

III. RESULTS AND DISCUSSIONS

When waves and currents coexist, their respective motions become coupled. To decouple this effect, we start with a comparative study on a fluid–structure interaction either induced by wave or current separately for both OC4 and IDEOL platforms. Because of their different geometric characteristics, it is expected to observe different dynamic motion responses. For the validation purpose, the comparison between our CFD results with experimental testing has been done for waves interaction with IDEOL platform. Other validations for this CFD tool can be found from our previous publications on (a) wave-structure interaction for floating platforms,[8,47] (b) wave energy devices,[44] and (c) the current–structure interaction for the OC4 platform with VIM studies.[31,48]

A. Response of the OC4 platform with current-only and wave-only conditions

Either current or wave interaction with OC4 platform is first studied, and the flow conditions are listed in Table III. Figure 5 displays the amplitude of the motion response in the current-only scenario along with the experimental data, in which IL component (A_{cx}) and CF component (A_{cy}) are plotted against flow velocities. They are calculated by multiplying the root mean square (RMS) displacement by $\sqrt{2}$ and then normalized with the characteristic length, which is D_s for the OC4 platform and W_B for the IDEOL platform.

In VIM analysis, the freestream velocity is commonly normalized using the natural frequency of the system (f_n). The reduced velocity is defined as $V_r = U/f_n D$, where U and D are the flow velocity and characteristic length of the structure. It can be rewritten as $V_r = UT_n/D$, where T_n is the natural frequency of structure. From a physical perspective, the numerator can be considered as the distance that the constant fluid flows over the structure in one natural vibration period. Thus, V_r is an indicator for the ratio between this distance and the structural dimension. In this study, cases with different V_r are achieved by only varying the flow velocity; meanwhile, Re number is also synchronized with V_r since they are both a representative of the flow velocity.
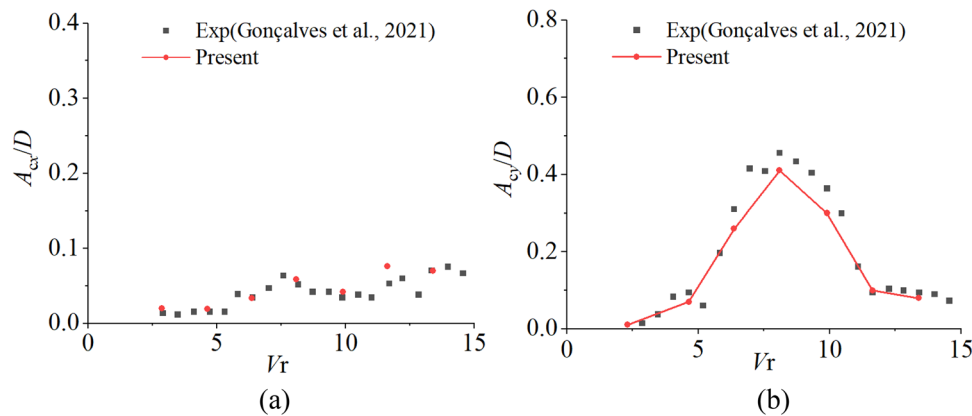

FIG. 5. Variation of the motion response amplitude with V_r in (a) IL direction and (b) CF direction for the OC4 platform with current-only condition.
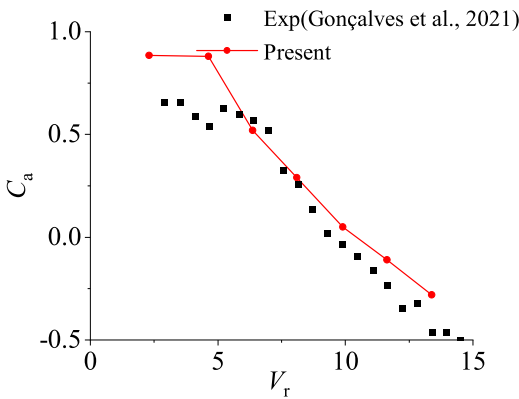
FIG. 6. Variation of added mass coefficient with V_r in CF direction for the OC4 platform with current-only condition.

The plot indicates that the CFD predictions are in good agreement with the experiments. The IL motion is significantly smaller compared to that of CF motion with A_{cx}/D being less than 0.1, indicating that the IL movement of platform is not dominant. The CF motion response shown in Fig. 5(b), however, reveals a very typical current–structure interaction VIM phenomenon. In particular, the lock-in region ranges from $V_r = 5$ to 10, in which the maximum A_{cy}/D characterized by VIM reaches a value of 0.41 at $V_r = 8.1$. At real sea conditions, the full-scale current velocity in the lock-in region can vary from 1.0 to 1.45 m/s. Therefore, it is expected to observe significant platform motion within this velocity range.

The added mass coefficient in the CF direction (C_a) also agrees well with the experiment as shown in Fig. 6, which is defined as $C_a = -R\left\{\dfrac{fft[F_y(t)]}{fft[\ddot{y}(t)]}\right\}/m$, where $F_y(t)$, y are the hydrodynamic force and displacement in the CF direction, respectively. $R()$ represents the real part of the complex number, and fft represents the fast Fourier transform (FFT) operator. The large and positive values of C_a with $V_r < 9.9$ denote the synchronization with the vortex shedding frequency. As the velocity increases, C_a decreases and becomes negative after $V_r > 9.9$, indicating the end of resonance.

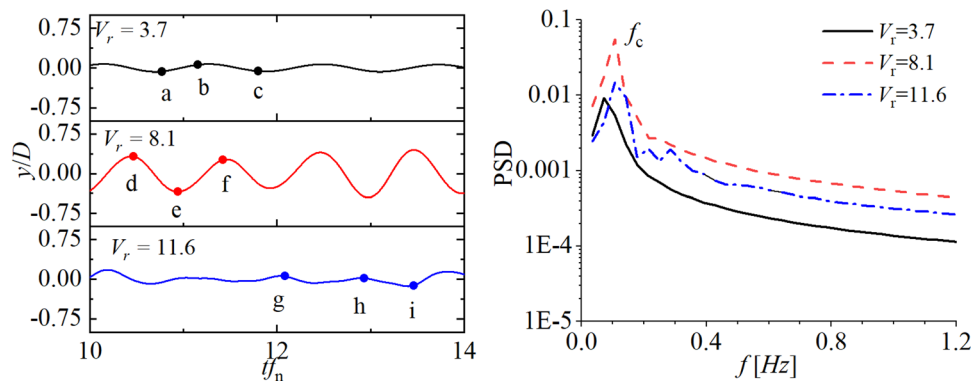The resonance in the lock-in region is also reflected by the time-series and the corresponding FFT analysis shown in Fig. 7, where a dominant VIM motion can be observed at $V_r = 8.1$ in the lock-in region. With a smaller $V_r = 3.7$, the periodic motion exists but has a lower frequency and smaller amplitude. At larger V_r beyond lock-in region, the amplitude is small but with higher-order frequency components.

The vorticity field is plotted and examined in Fig. 8 to reflect the typical vortex shedding associated with VIM phenomenon. It is seen that with the increase in V_r, the vorticity becomes stronger, and the flow field becomes more irregular. Within the lock-in region at $V_r = 8.1$ [Figs. 8(d)–8(f)], the vortices generate alternately from both sides of column and then shed from either side of the column at a frequency equal to the lock-in frequency f_n. An anti-clockwise vortex is observed when the platform reaches y_{min} in Fig. 7(e), and another anti-clockwise vortex is observed, while a clockwise vortex is shed when y_{max} at (f), revealing a typical 2P mode for the wake in VIM. At $V_r = 3.7$, no obvious vortex shedding is observed, which associates with a smaller motion in the CF direction.

In addition to the above-mentioned current-only condition, the wave-only condition is also examined for OC4 to set up a baseline model for the subsequent wave–current investigations. Figure 9 shows the predicted surge response amplitude operators (RAO) with various wave heights (H) and wave periods (T). It is seen that the RAO increases with T, as the platform's structure natural period aligns more closely with it, increasing the motion response. The RAO relationship with H is rather complex due to enhanced mooring forces with increasing H, as well as the higher nonlinearity with larger H. Therefore, the variation follows a nonlinear trend.

B. Response of the IDEOL platform with current-only and wave-only conditions

The IDEOL platform is analyzed starting with the current-only scenarios. The response amplitudes in IL and CF directions are shown in Fig. 10, with the parameters summarized in Table IV. It is seen that barge-type platform has an even smaller IL motion compared with the OC4 platform. The motion in the CF direction is also relatively smaller. For the largest reduced velocity of $V_r = 9.6$ ($U = 2.3$ m/s at full scale), the maximum A_{cy}/D is less than 0.2. Only at this largest V_r, the periodic platform motion characterized by VIM becomes notable, as shown in the time-series plots in Fig. 11.
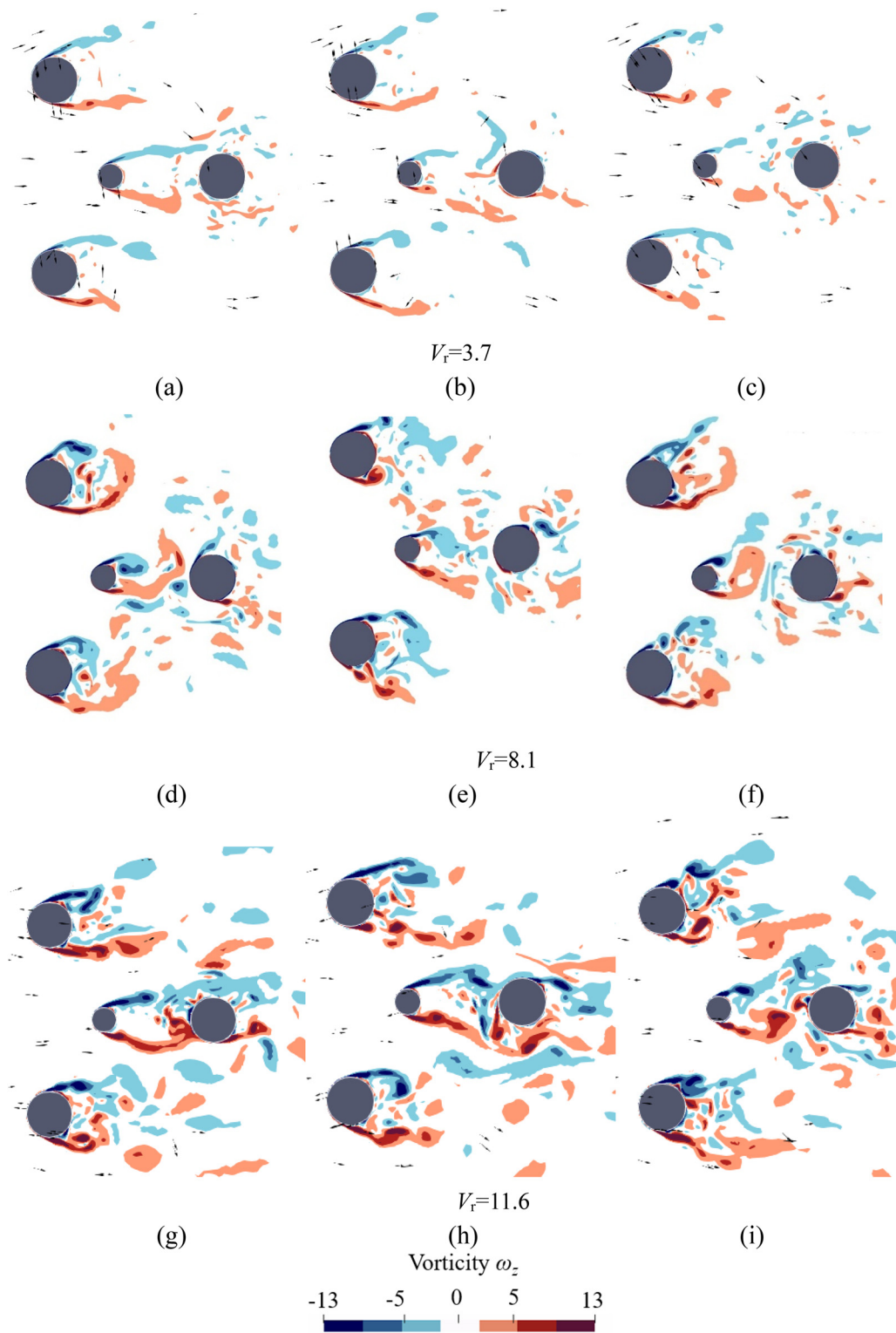

FIG. 7. Time-series and FFT analysis of CF motion response for $V_r = 3.7$, 8.1, and 11.6 for the OC4 platform with current-only condition.

FIG. 8. Contours of spanwise vorticity ω_z at the section with $z = -0.1$ m at the time instants shown in Fig. 7 at $V_r = 3.7$ (a)–(c), $V_r = 8.1$ (d)–(f), and $V_r = 11.6$ (g)–(i) for the OC4 platform with current-only condition.
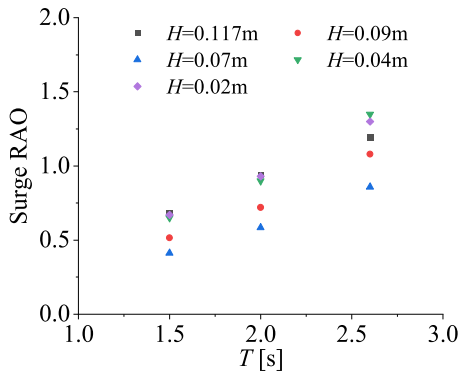
FIG. 9. Variation of surge RAOs with wave periods of the OC4 platform for wave-only condition.

TABLE IV. Wave and current parameters for IDEOL platform testing.

Wave parameters					
T (s) Scaled 1:50	1.6	1.8	2	2.2	2.4
T (s) Full-scale	11.3	12.7	14.1	15.6	17.0
Current parameters					
U (m/s) Scaled 1:50		0.20		0.26	0.32
U (m/s) Full-scale		1.4		1.8	2.3
V_r		6.1		8.0	9.6

Compared to the OC4 platform, the VIM phenomena are less profound, which might be due to several reasons.

First, the most pronounced vortex-induced motion (VIM) for the SS platform occurs around $V_r = 8.1$. Comparatively, for the IDEOL platform to experience significant VIM, it requires a much higher reduced velocity of at least 10.0 or even higher, as can be seen in Fig. 10. Thus, the VIM of IDEOL platform is not obvious. In addition, the aspect ratio of the IDEOL platform is 0.17, which is much smaller than that of 1.64 for the OC4 platform. This finding agrees with the research by Goncalves *et al.* that the response of CF motion of a cylinder weakens as its aspect ratio decreases. The VIM could be even negligible if the aspect ratio is less than 0.3.[18]

Then, the dynamic response of IDEOL platform for the wave-only condition is studied for a series of wave periods (Table IV). In the experiment, the wave heights varied from 2.5 to 7.5 m. In this validation, an intermediate wave height of $H = 5$ m is chosen. Figure 12 shows the predicted RAOs in comparison with the experiment (EXP) and numerical modeling (SIM) data. In the SIM studies, the potential-flow-based method is used, the hydrodynamic coefficient is obtained by Ansys Aqwa software, and the dynamic response is calculated using DNV-GL's Bladed software package[46] 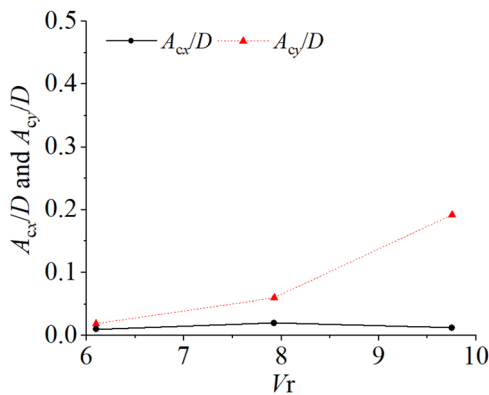to couple the hydrodynamic loads. The RAOs are normalized by the wave amplitude for heave and surge motions, while the pitch response is normalized by $kH/2$ Fig. 12.

For the wave periods studied, an averaged RAO for the surge and heave are typically 0.84 and 1.0, respectively, from CFD and EXP. However, the pitch RAO reveals an initial increasing and then decreasing trend. The peak RAO occurs at $T = 14.1$ s. It is evident that better agreement between the present CFD predictions and the experimental data has been reached than the results obtained from the potential-flow-based tool (SIM). One explanation for the improved accuracy of CFD modeling over the potential theory method is that the later linearizes the wave–air free-surface equation at the time-averaged positions; therefore, the nonlinear effect of fluid–structure interaction, represented by the changing wetted surfaces, is not very well captured.[46] As shown in Fig. 13, the green water can be observed clearly showing the changing wetted surface. Also, for the CFD modeling, tuning the viscous damping to fit the experiments is not required, which is usually needed for a viscous-modified potential flow model.

C. Response with combined current wave at different angles

In the above two sections for current-only and wave-only cases, it is observed that the VIM phenomena are more profound for a semi-submersible platform than a barge platform. Therefore, the following studies on a combined wave–current–structure interaction will be focused on OC4 semi-submersible platform.

It is well known that in a real sea state, current and wave do not always exist alone, and the extreme loading condition for a FOWT platform may occur with specific combinations of wave and current. In our previous study on a colinear wave–current condition,[38] it was found that the current-induced CF motion can be mitigated with the addition of waves, depending on V_r under investigation. This conclusion is consistent with others' findings. Some other studies also found that if the wave and current were non-colinear, the mitigation became less obvious.[49,50] To investigate this phenomenon, this section is dedicated to examining the impact of the angle of the flow direction between current and wave (θ) on the platform's dynamic responses. Three angles varying from $\theta = 0°$ to $90°$ are selected. Typical wave period and wave height are $T = 2.0$ s, $H = 0.09$ m. The current speed varies from 0.05 to 0.20 m/s, leading to the reduced velocity V_r ranging from 2.3 to 11.6, as shown in Table V.

The responses of platform are shown in Fig. 14 with different angles. Given a combined wave–current condition, the IL motion varies a little with reduced velocity, indicating that varying current
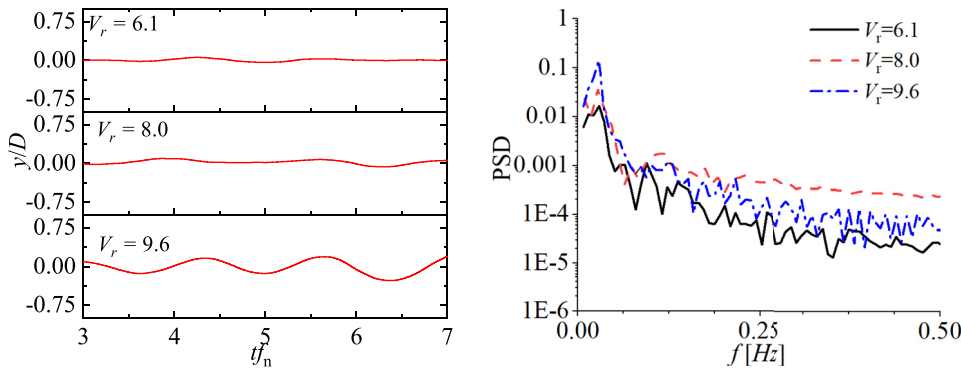

FIG. 10. CF and IL motion amplitude vs reduced velocity for IDEOL platform with current-only condition.

FIG. 11. Time series and FFT analysis of CF motion response for $V_r = 6.1$, 8.0, and 9.6 for IDEOL platform with current-only condition.

speed does not affect IL motion significantly, as shown in Fig. 14(a). However, the IL motion is noticeably impacted by angles variation (θ). In fact, with $\theta = 0°$, A_x/D is the largest and close to A_w in the wave-only cases, while $\theta = 90°$, A_x/D is the smallest and close to that in the current-only cases. Unlike the above IL response, CF motion varies significantly with reduced velocity and the peak values can be clearly captured [Fig. 14(b)]. As the angle θ increases, A_y/D increases across all V_r. Therefore, for safety design purposes, it is recommended to pay more attention to those cases with $\theta = 90°$. Beyond the lock-in region, with $\theta > 0°$, A_y/D are greater than those observed in the current-only
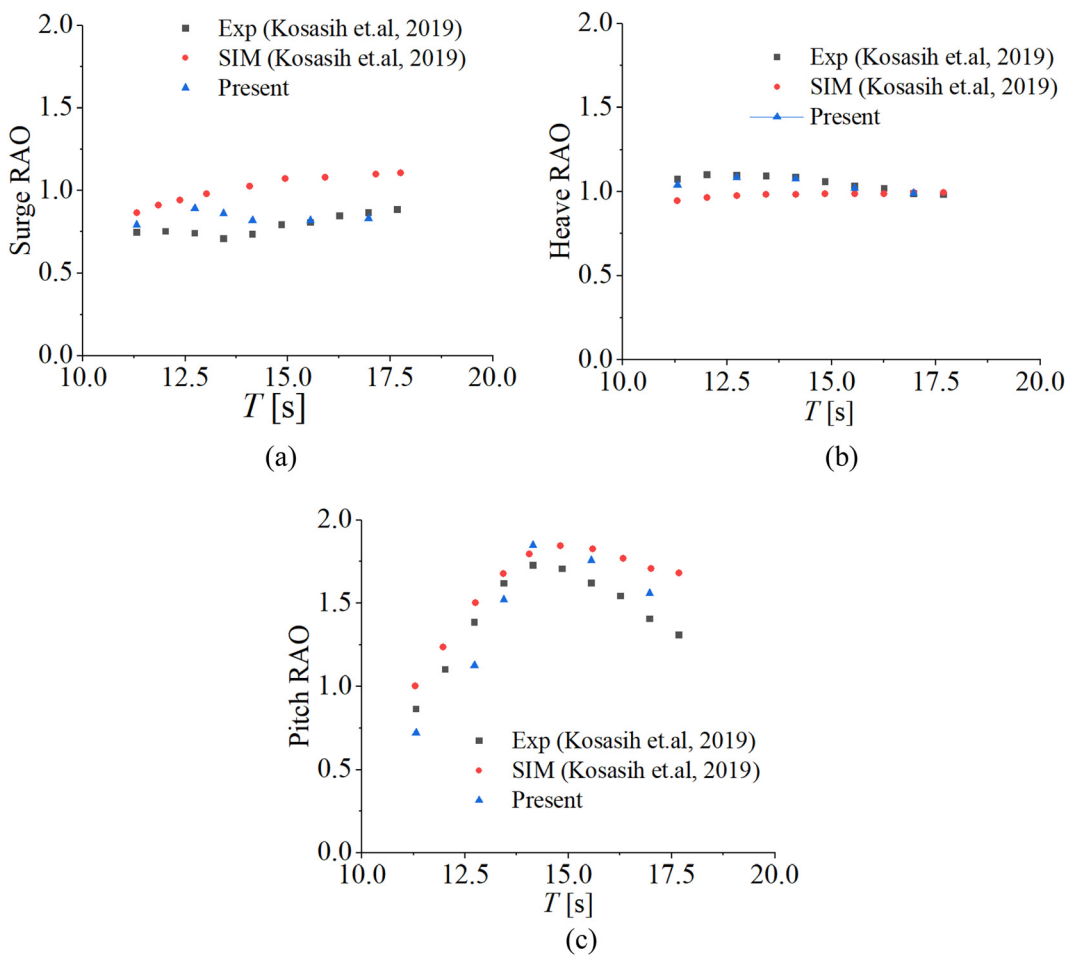

FIG. 12. Variation of RAOs with wave periods with $H = 5$ m for (a) surge; (b) pitch; and (c) heave for IDEOL platform with wave-only condition.
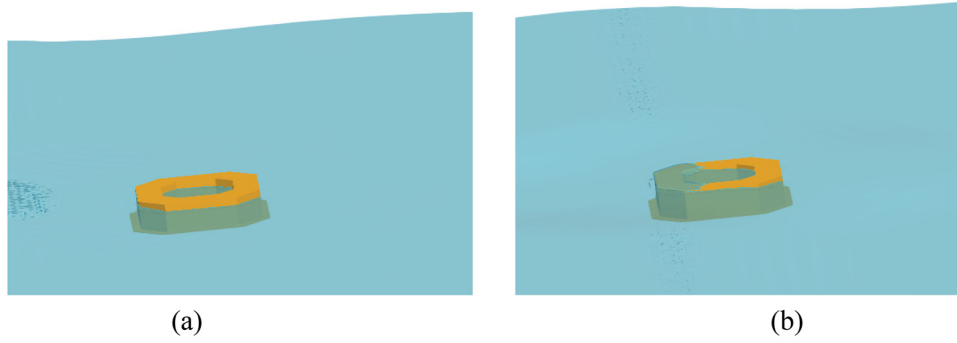
FIG. 13. Wetted surface changes on the IDEOL platform at different sampling time periods: (a) $t/T = 3.5$ and (b) $t/T = 4.0$ with $H = 5$ m and $T = 14.1$ s.

TABLE V. Current parameters for wave–current interaction with the OC4 platform on the effect of angles.

U (m/s) Scaled 1:73	0.05	0.08	0.11	0.14	0.17	0.20
U (m/s) Full-scale	0.43	0.68	0.94	1.20	1.45	1.70
Vr	2.30	3.7	4.6	8.1	9.9	11.6

cases and close to A_w. However, within the lock-in region, with increasing θ to 90°, A_y/D is always larger than that of either wave-only or current-only. The large CF motion in this wave–current condition is induced by the non-zero wave–current angle. As the velocity

components along the y axis increase with the angle, CF response increases due to the enlarged inertia wave force acting on the platform. In addition, the flow field and VIM are altered with a combined wave-current interaction.

To examine the individual effect of current and wave on the motion response, the above CF motion (A_y/D) is decomposed as follows:

$$a_c = |Y(f_c)|, \tag{15a}$$
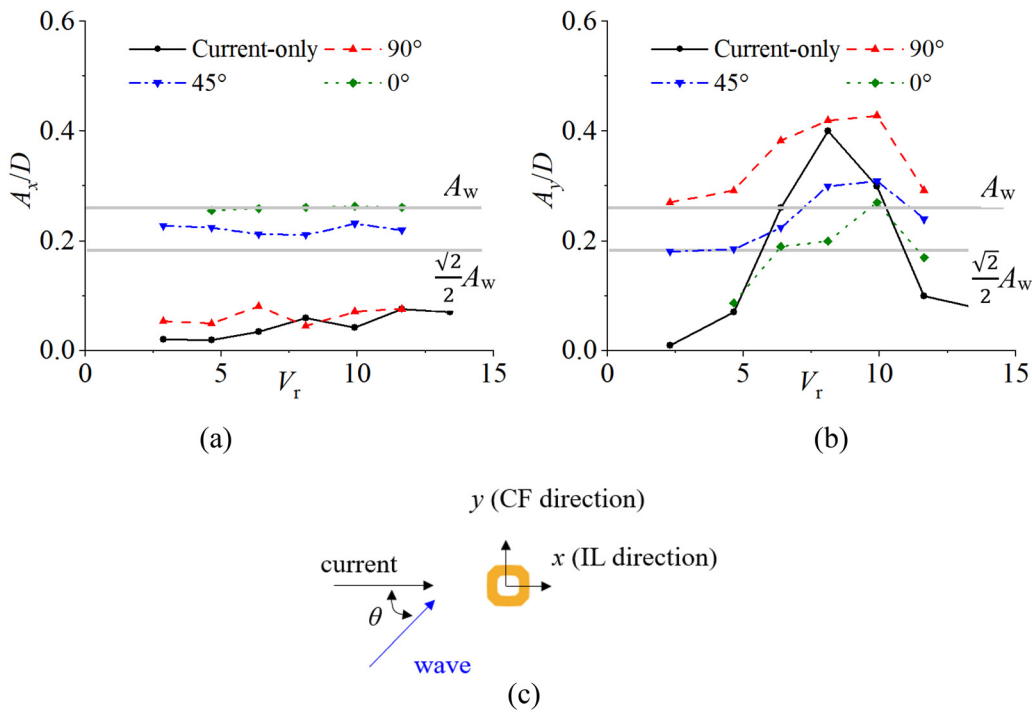
and

$$a_w = |Y(f_w)|, \tag{15b}$$

FIG. 14. Variation of motion response in wave–current condition with V_r and θ ($H = 0.09$ m and $T = 2.0$ s): (a) IL direction, (b) CF direction, and (c) is the sketch of the direction of current and wave. The horizontal line (A_w) is the amplitude shown in Fig. 9 for wave-only test, and $\sqrt{2}/2A_w$ denotes the motion components at $\theta = 45°$.
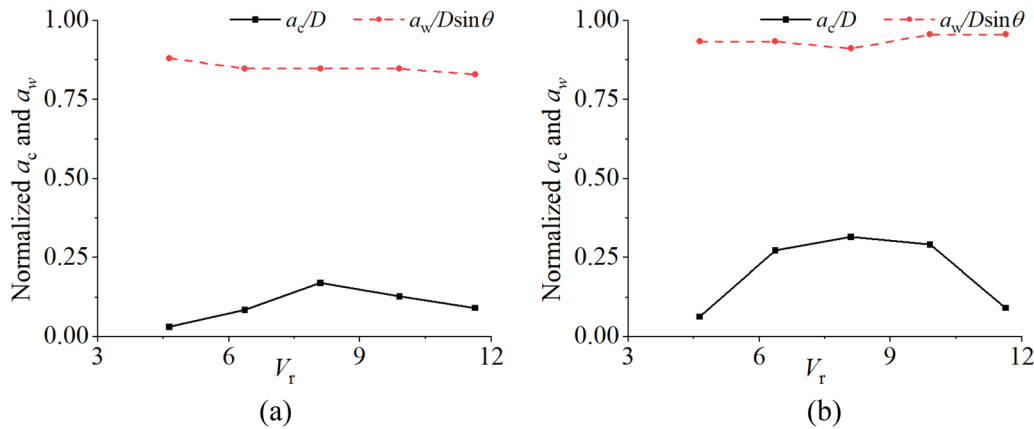
FIG. 15. Variation of decomposed CF motion excited by current (a_c) and waves (a_w) ($H = 0.09$ m and $T = 2.0$ s) at angles of (a) 45° and (b) 90°; a_c is normalized by characteristic dimension D, and a_w is normalized by wave amplitude multiplied by $\sin(\theta)$.

where $|Y(f)|$ is the FFT of CF motion. a_c and a_w are the motion amplitudes induced by current and wave, and f_c and f_w are the peak frequency corresponding to VIM and the wave. The decomposed a_w and a_c for $\theta = 45°$ and 90° are shown in Figs. 15(a) and 15(b). For both angles, a_w almost remains unchanged with V_r. As a result, the contribution of wave to the total response is nearly constant with varying V_r.

However, the variation of a_c with V_r resembles the pattern of current-only cases, with the peak amplitude occurring at $V_r = 8.1$ and decreasing beyond this V_r. This indicates that the VIM effect still exists even with waves. Hence, the response peaks in the wave–current cases depicted in Fig. 14 are primarily due to the current's contribution within the lock-in region. A comparison between Figs. 15(a) and 15(b) indicates that larger θ leads to an amplified VIM. It is also worthwhile to note that with a larger angle, the a_c near the peak value at $Vr = 8.1$ also increases, which means that the VIM becomes significant for a wider range of reduced velocities with the addition of waves.

The effects of angle are also reflected in dominant frequencies, as analyzed in Fig. 16. For current-only cases, f_y increases with V_r and locks onto f_c in the lock-in region, leading to a large motion response. For cases with $\theta = 0°$, f_y is the same as that of current-only. However, for those with $0° < \theta < 90°$, outside the lock-in region, f_y is close to f_w
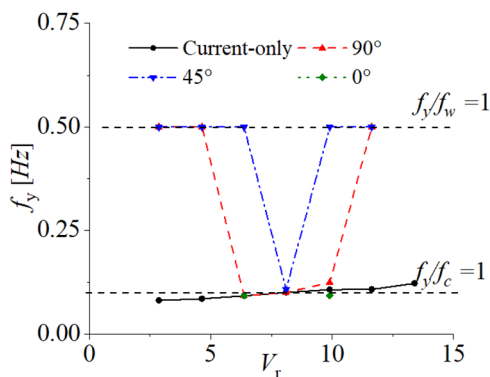
indicating the platform's motion is dominated by waves. Within the lock-in region $f_y = f_c$, the resonance occurs. With an increasing θ, the lock-in region becomes wider, revealing a more vulnerable platform due to large-scale motions under a wide range of current velocity. The time-series distribution of y/D and their FFT analysis displayed in Fig. 17 reinforce the above observations. In fact, two dominant frequencies appear in relation to f_c and f_w. Outside lock-in region, the low-frequency components are not as prominent compared to the high-frequency components. Within the lock-in region, the low-frequency component is substantially large and increases with angles. In addition to the above dominant frequencies, other spikes are also noted, which might be caused by the nonlinear coupling between the vibration of platform and fluid flow. The difference frequency $f_{diff} = f_w - f_c$ and sum frequency $f_{sum} = f_w + f_c$ exist, although with a relatively small magnitude, which is also noticeable in the cases with 90° with heir magnitudes increasing with angle.

Figures 18 and 19 present vorticity field under the combined waves and current conditions for $\theta = 0°$ and $\theta = 90°$ at $V_r = 8.1$. Unlike the current-only cases in Fig. 8, the fluid field with waves for $\theta = 0°$ in Fig. 18 becomes chaotic and its precise pattern is hard to discern. It displays the characteristics of cylindrical structures interacting with both steady and oscillatory flow. The steady flow leads to a typical VIV vortex shedding, while the oscillatory flow leads to a different shedding pattern. The specific appearance of pattern highly replies on the Keulegan–Carpenter number (KC number),[51] which describes the relative importance of the drag forces over inertia forces in an oscillatory flow. In a pure oscillatory flow scenario, VIM only occurs at a large KC, by the hydrodynamic lift force in the CF direction,

$$KC = \frac{U_M}{f_w D}, \tag{16}$$

where U_M is the maximum flow velocity in the IL direction. At time instants of (c) to (e), the vortices are shed from both sides of offset columns (the larger columns) and move downstream, having a symmetric pattern. The vortex shedding frequency of this process is 1/2 s, much smaller than the lock-in frequency, but is identical to the wave frequency f_w, indicating that the symmetric vortex pair is dominated by oscillatory flow/waves. When oscillatory flow passed a cylinder at a
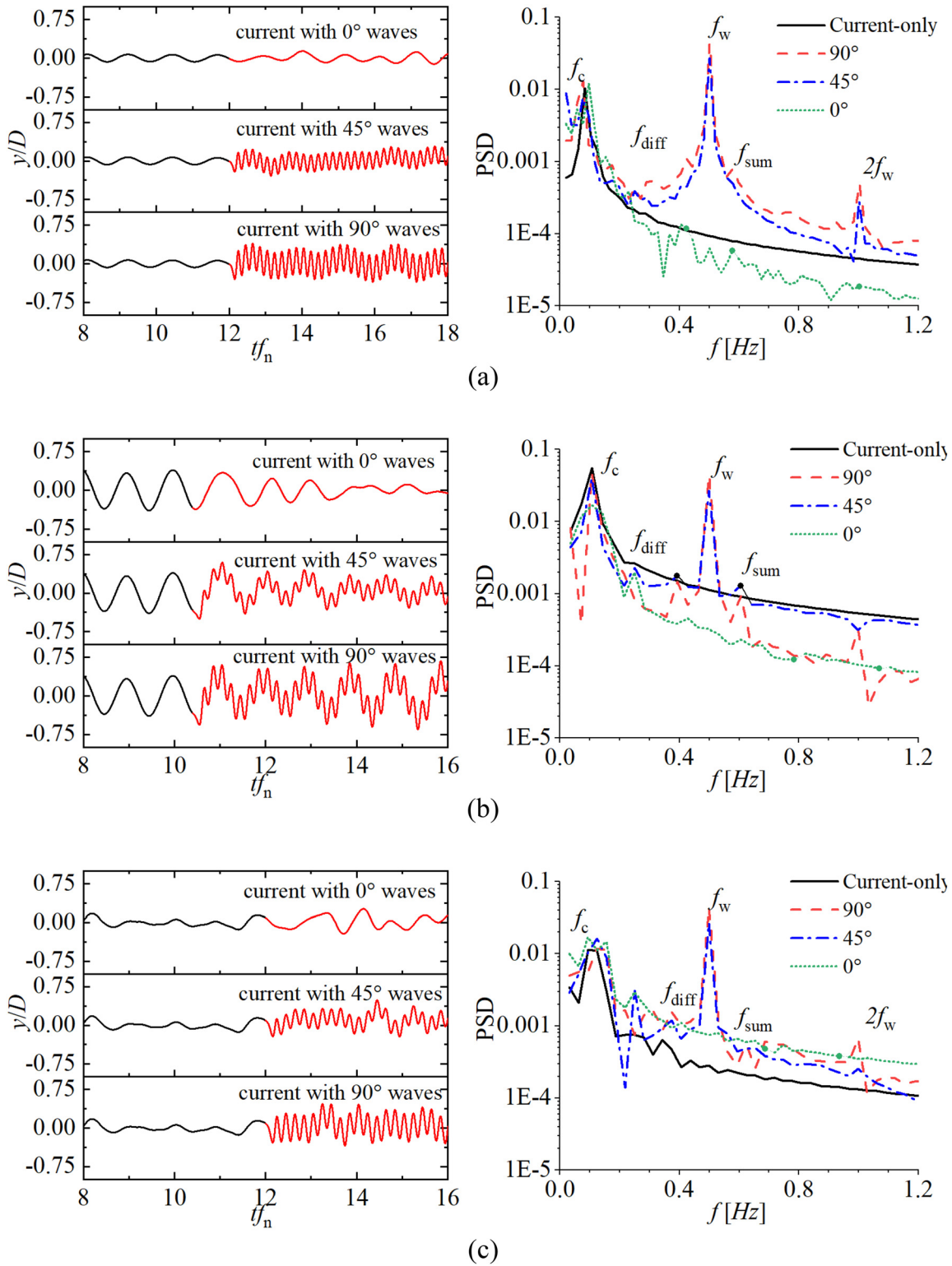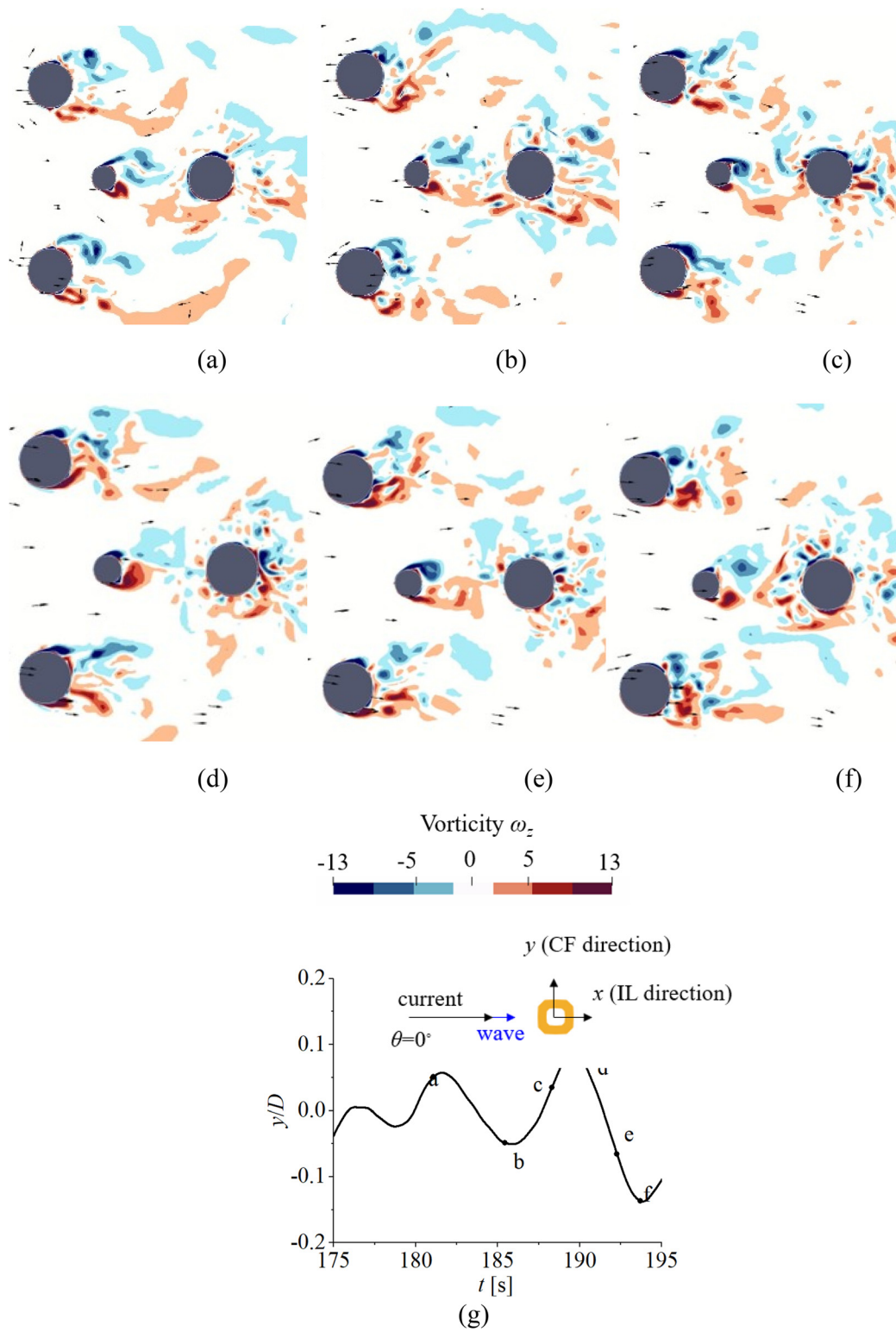

FIG. 16. Variation of dominant frequency with V_r ($H = 0.09$ m and $T = 2.0$ s).

FIG. 17. Time-series and FFT analysis of CF motion response in wave–current condition ($H = 0.0$ 9 m and $T = 2.0$ s) of (a) $V_r = 4.6$; (b) $V_r = 8.1$; and (c) $V_r = 11.6$. In the time series, black line represents the response caused by the current only, while red line indicates the addition of waves to the current.

FIG. 18. Contours of spanwise vorticity ω_z at the section with $z = -0.1$ m and $\theta = 0°$ in wave–current condition ($H = 0.09$ m and $T = 2.0$ s) at different time instants at $V_r = 8.1$ for (a) to (f), and (g) is the corresponding time series, on top of which is the sketch of angle between wave and current.
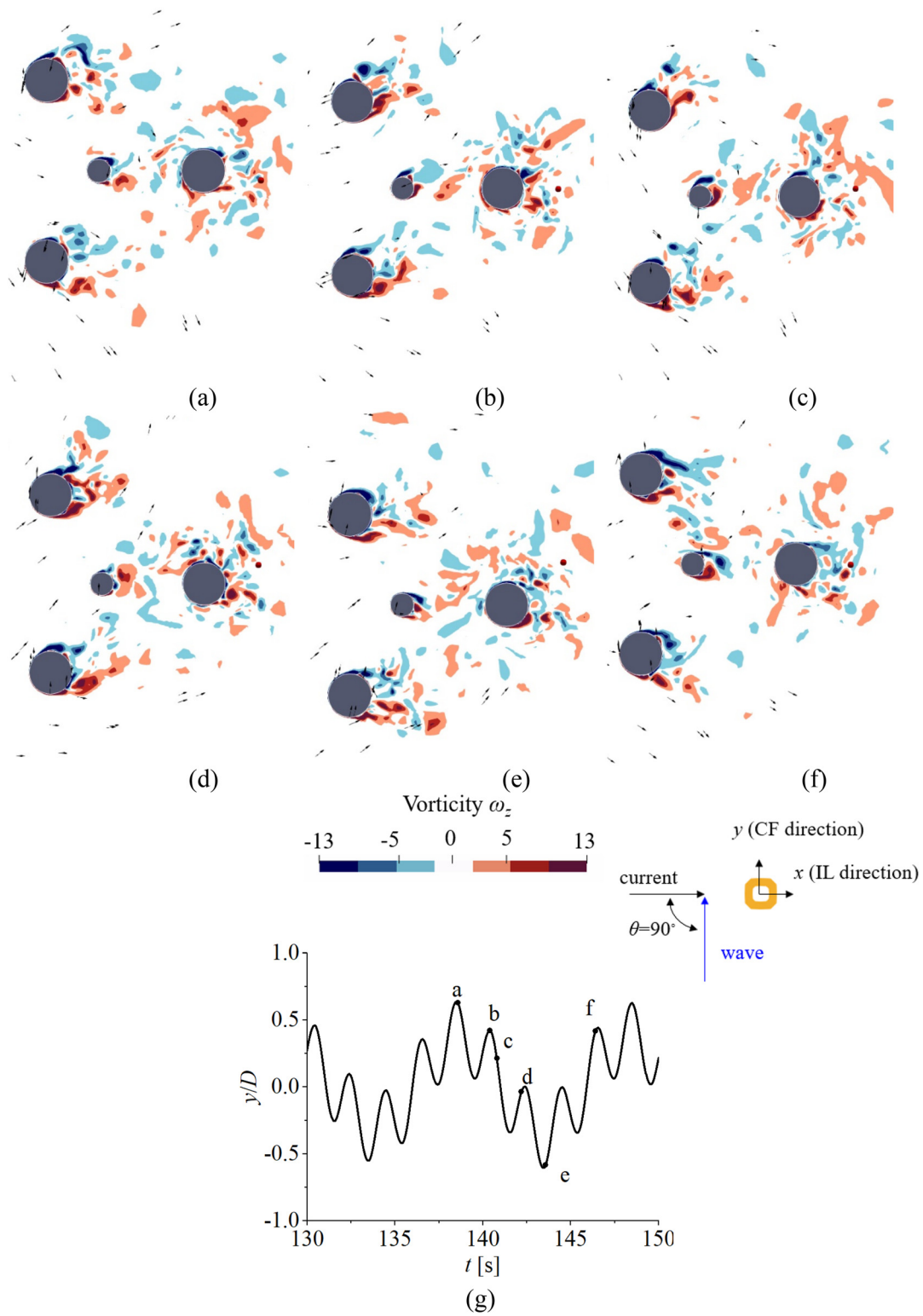
FIG. 19. Contours of spanwise vorticity ω_z at the section with $z = -0.1$ m and $\theta = 90°$ in wave–current condition ($H = 0.09$ m and $T = 2.0$ s) at different time instants from (a) to (f), at $V_r = 8.1$, and (g) is the corresponding time series, on top of which is the sketch of angle between wave and current.
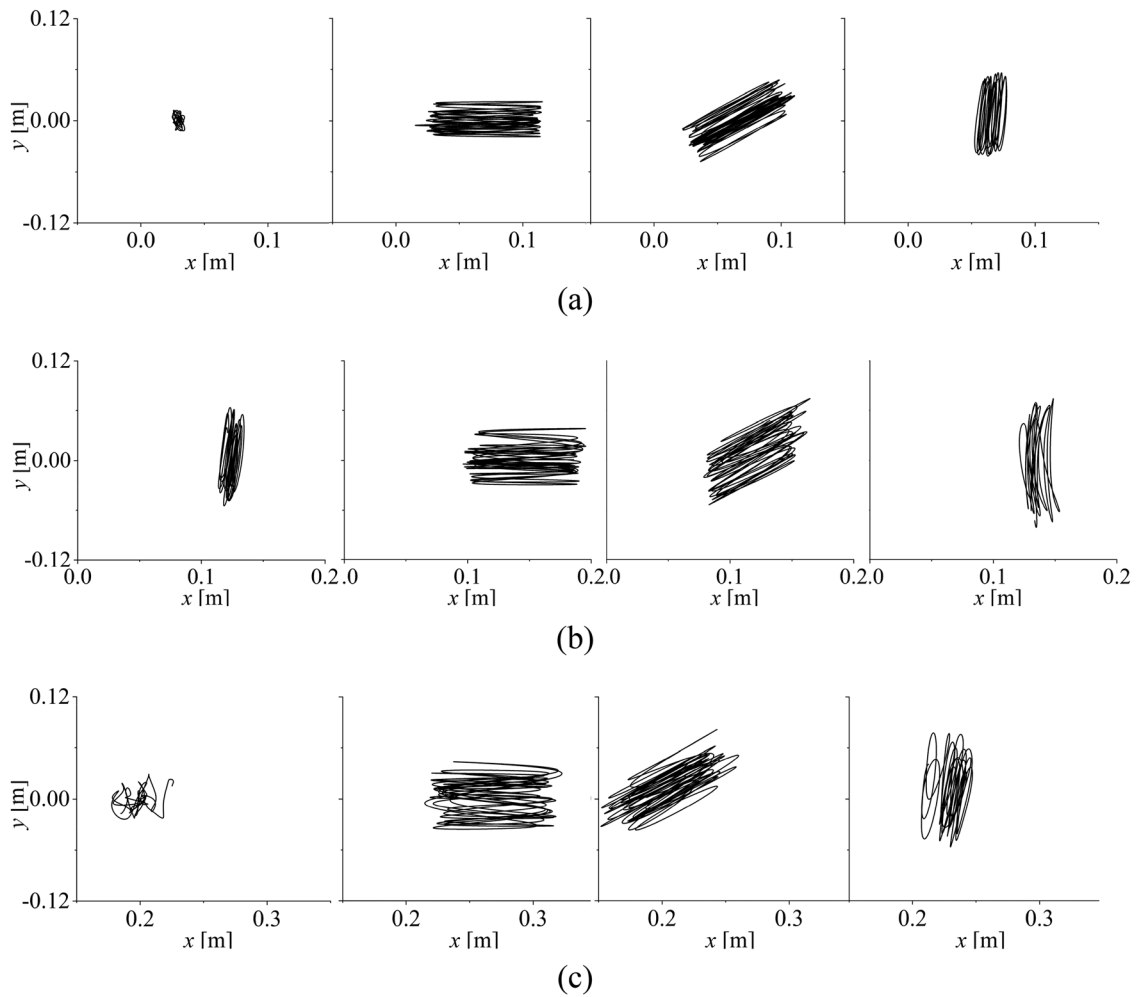
FIG. 20. The trajectory of platform with current-only, wave–current condition ($H = 0.09$ m and $T = 2.0$ s) with $\theta = 0°$, $45°$, and $90°$ at (a) $Vr = 4.4$, (b) $Vr = 8.1$, and (c) $Vr = 11.6$.

small KC number between 1.6 and 4.0, the vortex separation begins to occur in the form of a pair of symmetric attached vortices,[16] as also observed for offset column with $KC = 2.1$. Two vortex pairs generate in one cycle, one from the previous half period where flow passes in one direction. Another pair generate from the second half period when the oscillatory direction reverses. In the present case for wave-steady current, only one vortex pair generates within one cycle and is flushed downstream, showing a 2T mode [Fig. 18(b)], where three vortices are seen to be shed from the lower offset column. This mode was also observed in Zhao's study for steady and oscillatory current around a cylinder.[52] The 2T mode is observed when the motion displacement reaches its maximum at the steady flow-dominated frequency. Away

from this time period, the double pair mode dominates [Figs. 18(a) and 18(d)]. For the central smaller column, the vortex shedding is also dominated by waves but with a different pattern than the offset column. The KC number for the central column is 3.8, and the vortex is seen shed alternatively from one side of the column with an asymmetric pattern. Typically, this pattern occurs for a pure oscillatory with a cylinder when $KC > 4.0$.[16] However, in cases where a steady flow is present, this pattern is also observed at a smaller KC number.

It should be noted that the symmetric vortex pair does not provide net force along the CF direction, but it interferes with the vortex formed by the steady flow. Moreover, the flow in the $-x$ direction caused by the waves mitigates the generation of a complete vortex due

TABLE VI. Parameters for wave–current–platform interaction with the OC4 platform on the effect of wave conditions with $\theta = 90°$.

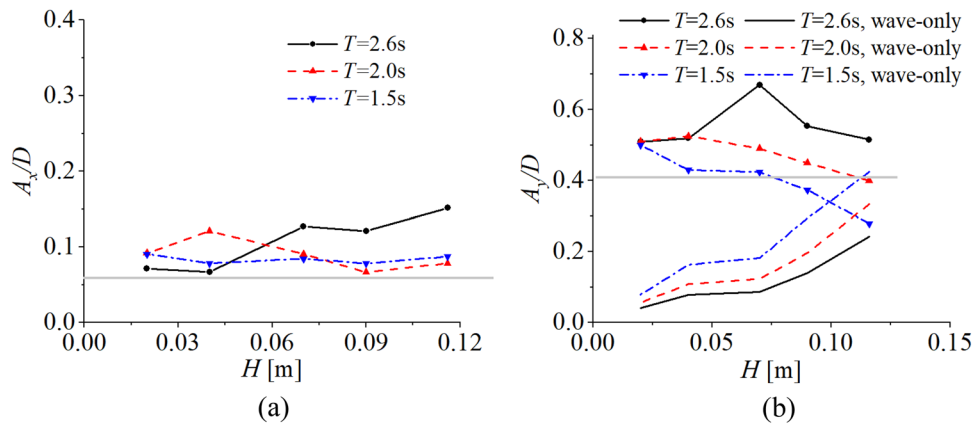| Wave height H (m) Scaled 1:73	0.116	0.09	0.07	0.04	0.02	Wave period T (s) Scaled 1:73	1.5	2.0	2.63
H (m) Full-scale	8.4	6.5	5.1	3.0	1.5	T (s) Full-scale	12.8	17.6	22.6

FIG. 21. Response amplitude in wave–current condition with different wave heights and periods along (a) IL direction and (b) CF direction, with $\theta = 90°$. The gray line indicates the motion amplitude with current-only condition.

to a steady current, leading to a possible reduction in the cross-flow motion.

Compared to the cases with $\theta = 0°$, the vortex field for $\theta = 90°$ in Fig. 19 shows more asymmetric characteristics. Since the waves propagate along the y axis, the flow along the x axis is less affected. As a result, when a vortex forms, it is periodically stretched and carried by oscillatory flow in the CF direction, causing it to split into smaller vortices. At $(y/D)_{max}$ and $(y/D)_{min}$ in Figs. 19(a) and 19(e), a large vortex is generated on one side of the offset column, but breaks down into small eddies. The vortex from the central small column presents a 2S mode with one clockwise and one counterclockwise vortex detaching from the central column within one cycle. Moreover, the shed vortex not only moves downstream but also along the CF direction, bringing it closer to the platform and increasing the chances of encountering between the clockwise and counterclockwise vortices, thereby changing the motion frequency. This is clearly depicted from Figs. 19(b) and 19(c), where V_y is positive, while V_y is negative at Fig. 19(f). It is clearly indicated that when the wave and current are colinear, oscillatory flow mitigates the generation of a complete vortex due to current; thus,

the VIM is mitigated. The disturbed vortex field by the symmetric vortex from the oscillatory flow contributes to this trend.

The platform motion trajectory with different θ and V_r is shown in Fig. 20. For current-only cases, the platform experiences significant motion displacement within the lock-in region at $V_r = 8.1$. The predominant motion is along the y axis, and the movement along the x axis is limited. This pattern of movement is similar to that in the study on a four-square column semi-submersible platform, where a typical eight-shaped trajectory is not found.[25]

D. Response for $\theta = 90°$ with different wave parameters

Previous studies on colinear wave–current–structure interaction indicated that the CF response was not only affected by the reduced velocity, but also influenced by the wave parameters, i.e., the wave height and wave period (Gonçalves et al.[35,36]). In addition, our findings from Sec. III C for various θ values reveal that the largest CF motion occurs at $\theta = 90°$. In this section, the investigation is focused on the study of wave–current–platform interaction at $\theta = 90°$ for a
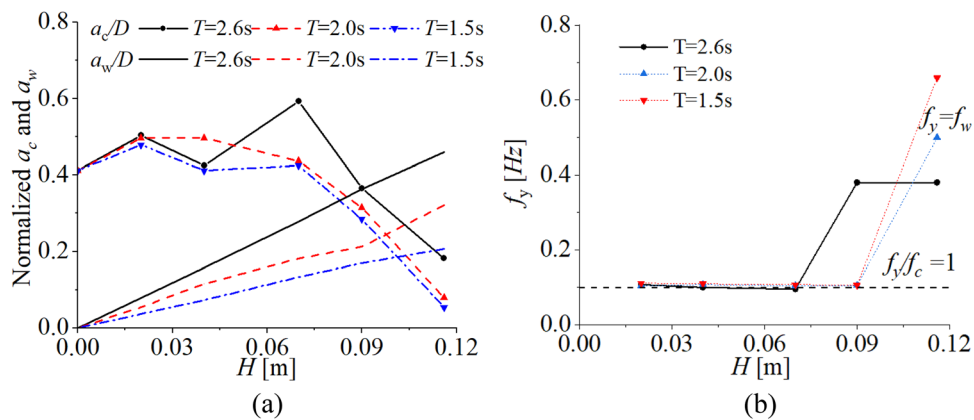

FIG. 22. (a) Decomposed motion amplitude excited by current and waves and (b) dominant frequencies at $V_r = 8.1$ with different wave parameters.
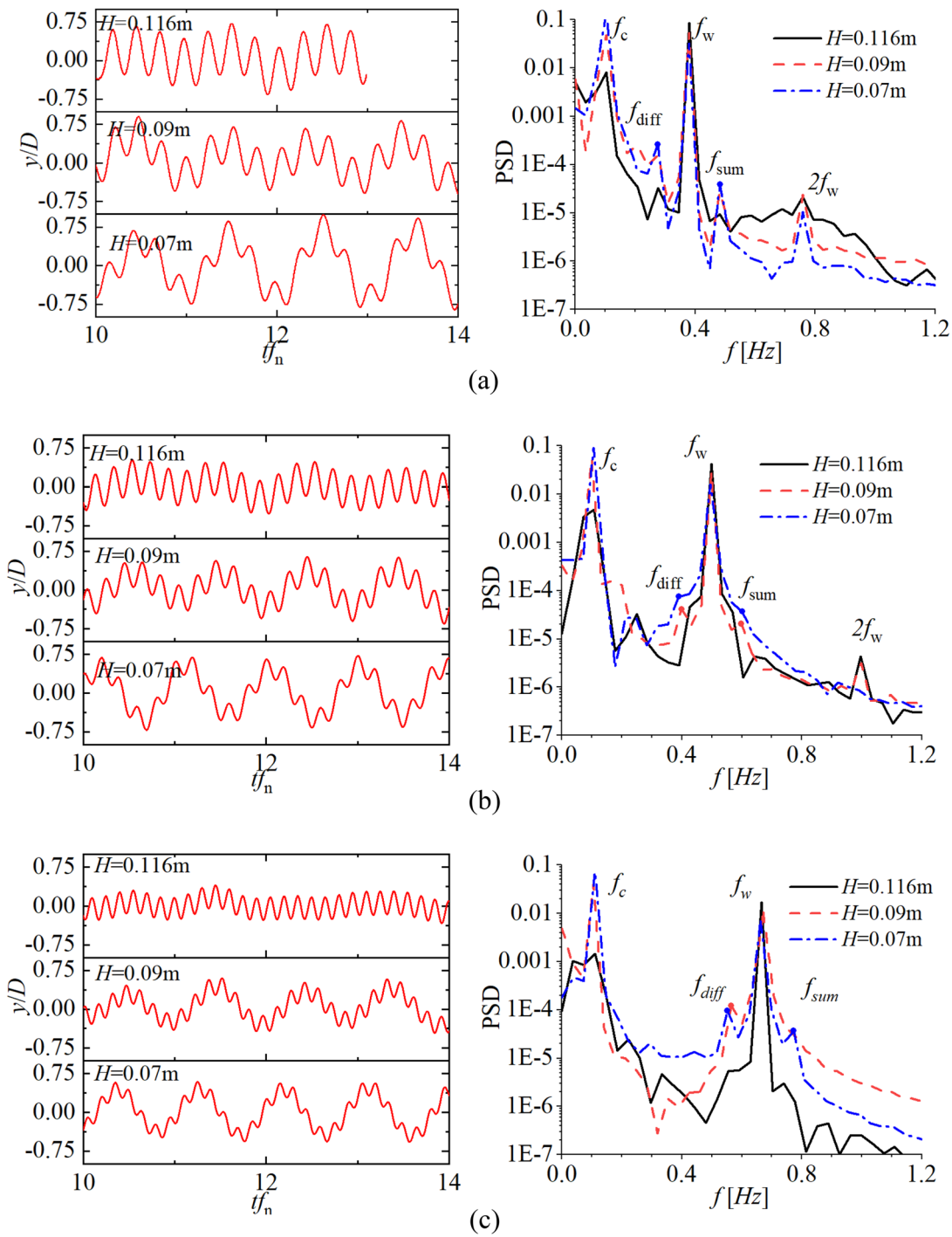
FIG. 23. Time-series and FFT analysis of CF motion response in wave–current condition with $\theta = 90°$ at $V_r = 8.1$ with (a) $T = 2.6$ s; (b) $T = 2.0$ s; and (c) $T = 1.5$ s.

series of wave heights and wave periods (Table VI). The reduced velocity is fixed at $V_r = 8.1$, where the strongest VIM occurs.

The effect of wave parameters on the platform's response is shown in Fig. 21. It is seen that the IL motion is relatively small compared with the large platform dimensions. The overall CF motion is larger than that observed in the current-only cases and increases with wave period T. The motion response is also influenced by wave height H. As H increases, A_y/D approaches that of

wave-only cases. A_y/D decreases monotonically with H for $T = 1.5$ s. However, peaks are observed for $T = 2.0$ s and $T = 2.6$ s, and the peak A_y/D is seen at $H = 0.04$ and 0.07 m, respectively. This concludes an important finding, e.g., waves with a small wave height

may also lead to large platform motion under the wave–current condition.

This can be further inferred by decomposing the motion amplitude shown in Fig. 22(a). For cases with small $H < 0.06$ m, the motion
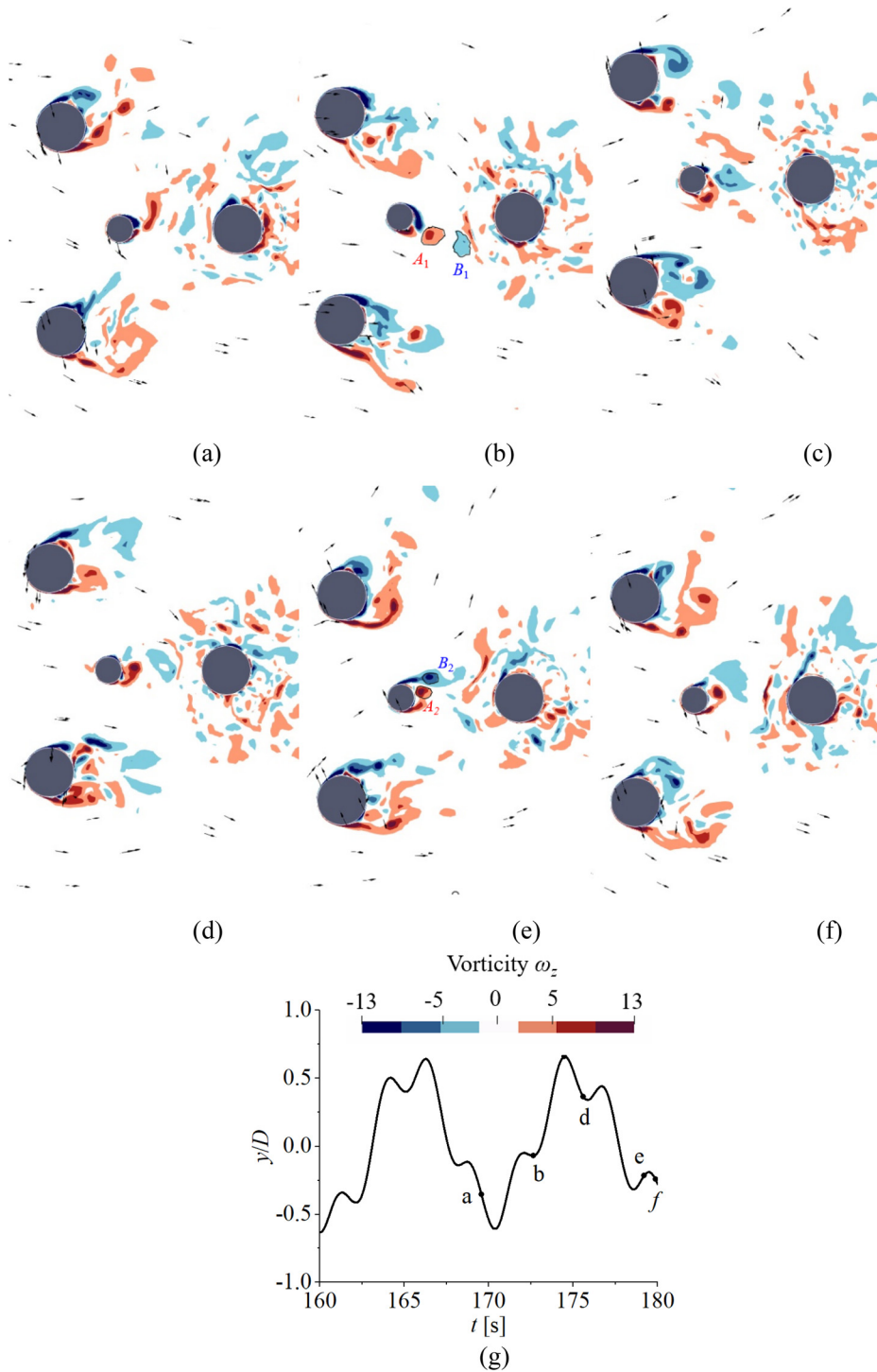

FIG. 24. Contours of spanwise vorticity ω_z at the section with $z = -0.1$ m with $T = 2.6$ s and $H = 0.04$ m in wave–current condition with $\theta = 90°$ at $V_r = 8.1$, at different time instants from (a) to (f), and (g) is the corresponding time series.

induced by current, indicated by a_c, varies between $0.4 < a_c/D < 0.5$, which is larger than that observed in current-only cases, indicating an enhanced VIM effect. However, for $H > 0.06$ m, a_c decreases significantly with increasing H, indicating a mitigated VIM effect by waves.

Meanwhile, a_w becomes dominant after $H > 0.11$ m, and the motion is locked onto f_w rather than f_c, as shown in Fig. 22(b). The shift in the predominant influence from currents to waves can also be observed from the time histories of y/D and FFT plots in Fig. 23. As H increases,
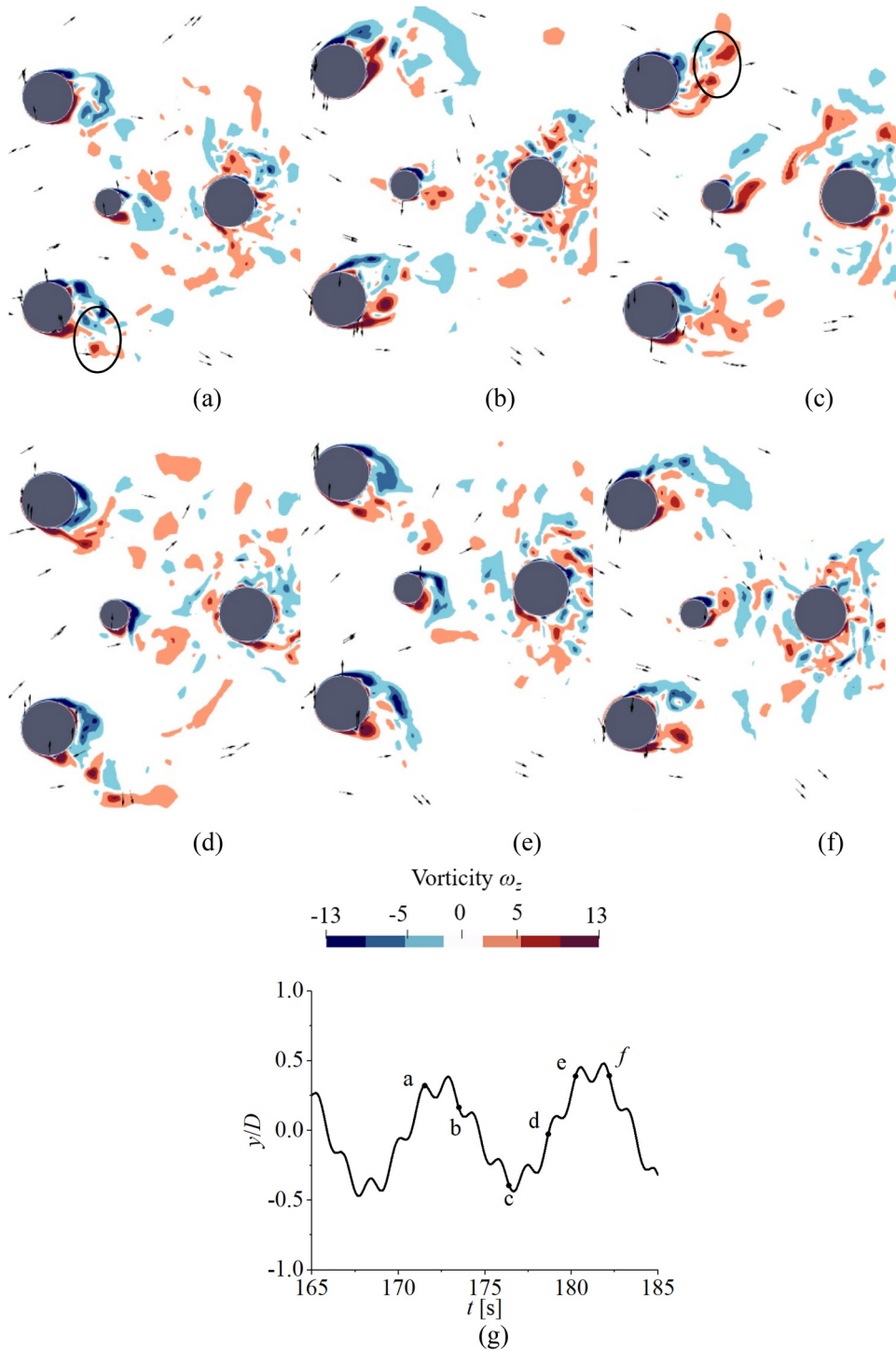

FIG. 25. Contours of spanwise vorticity ω_z at the section with $z = -0.1$ m with $T = 1.5$ s and $H = 0.04$ m in wave–current condition with $\theta = 90°$ at $V_r = 8.1$, at different time instants from (a) to (f), and (g) is the corresponding time series.

the low-frequency motion induced by current becomes less prominent. The FFT analysis indicates the appearance of difference frequencies and sum frequency components, especially for $\theta = 90°$. These frequencies are only excited when the contribution of current and wave to the system's energy is roughly equivalent. As H increases, the energy at f_c weakens, causing above two frequencies to become less significant.

The differences in wave parameters are also reflected in the vorticity field shown in Fig. 24 for $H = 0.04$ m. Compared with larger $H = 0.09$ m in Fig. 19, the vortex herein are less disturbed by waves, thus leading to a larger CF motion response. The vortex shedding appears at the 2P mode, with two pairs of vortices shed in one cycle, such as the vortex A_1 and B_1 at instant b and A_2 and B_2 at instant e. As the wave period decreases, the vortex flow exhibits greater levels of turbulence and disorder, as seen from Figs. 25(a) and 25(c). Additionally, the vortex motion is observed to occur in close proximity to the structure with smaller T.

According to Iwagaki, and Asano,[53] the velocity ratio can be an important parameter in the study of a combined wave–current environment. It is defined as

$$\alpha' = \frac{\sigma_U}{\sigma_U + U}, \quad (17)$$

where U and σ_U are the current velocity and the particle velocity amplitude in wave. With this definition, α' quantifies whether a flow is viscous or inertial dominant, and thus, $\alpha' = 1$ and 0 represent a wave-only or a current-only scenario, respectively. A previous study by Gonçalves et al.[35,36] for a semi-submersible platform revealed that VIM is governed by both viscous and inertia forces. The threshold between the viscous and inertia zones can be quantified by

$$KC = \frac{1 + C_a}{C_D} \pi (\alpha')^2, \quad (18)$$

where C_a and C_d are the added mass and drag coefficient, which are 0.63 and 0.61 for the OC4 DeepCwind platform. respectively.[54]

Figure 26 plots velocity ratio (α') as a function of KC number with $\theta = 90°$. For the wave parameters examined, most cases are within a regime where VIM is obvious, thus associated with a large CF
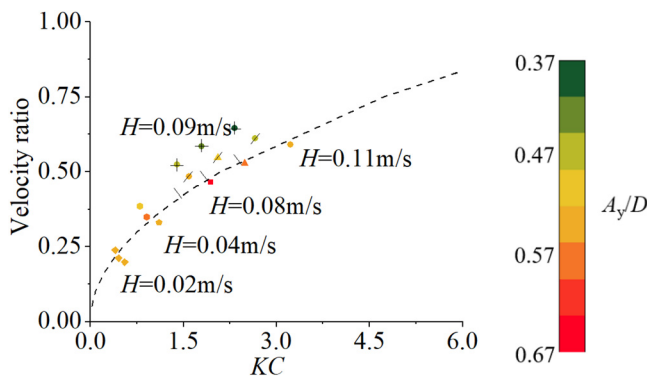

FIG. 26. α'-KC plot with $\theta = 90°$ denoting predominant region of either drag or inertia force in wave–current condition for the OC4 platform. The point with color denotes CF motion response. The black line denotes the threshold between drag range and inertia range.

TABLE VII. IEF with different wave parameters for $\theta = 90°$ and $V_r = 8.1$.

H (m)/T (s)	1.5	2	2.6
0.02	1.02	1.09	1.13
0.04	0.75	1.01	1.06
0.07	0.72	0.92	1.35
0.09	0.53	0.74	1.01
0.116	0.34	0.54	0.79

motion. For those falling into inertia force regime, the response is mainly wave-dominant.

It should be noted that falling in the drag zone does not correspond to larger motion. For instance, the cases with V_r beyond the lock-in region have a very small velocity ratio and should be located in the drag zone. However, the absence of resonance leads to a smaller VIM amplitude. The interaction effect factor (IEF) is normally used to which is defined as

$$IEF = \frac{stddev(y_{wc})}{stddev(y_w) + stddev(y_c)}, \quad (19)$$

where y_{wc} is the CF motion in the wave–current combined environment, y_w and y_c are the CF motion in wave and current independently, and $stddev$ means the standard deviation function. IEF can be viewed as the ratio between the amplitude of y_{wc} and $y_w + y_c$. For larger H and smaller T, the IEF becomes lower than 0.75 as shown in Table VII, suggesting that the interaction of waves and current mitigated the sum of their original motion. For small H and large T, the IEF is the largest and close to 1, which means that the motion can be considered as the sum of the motion in waves and current alone. For some cases, the IEF exceeds 1 and reaches 1.35 when $H = 0.07$ m and $T = 2.6$ s, indicating that the motion is enhanced by the wave–current interaction. Special attention should be paid to those cases when the extreme conditions for the platform are considered during the design process.

IV. CONCLUSION

This study explores the fluid–structure interaction of floating offshore wind turbines under various scenarios, including wave-only, current-only, and wave–current conditions in which the motion response is one of the main concerns. The CFD package OpenFOAM with further developed models is used for the simulation. To reduce the computational size for wave–current cases, a hybrid mesh and active wave absorbing scheme are utilized. The comparison study shows that a semi-submersible platform has a larger aspect ratio, exhibits a larger cross-flow (CF) motion, and experiences the lock-in phenomenon for the reduced velocities considered. Conversely, a barge platform, with a larger cross-surface area and low aspect ratio, shows a much smaller motion. Obvious vortex-induced motion (VIM) is not seen with selected V_r, indicating that there is little chance for a floating barge platform undergoing a lock-in phenomenon.

The angle between the directions of wave and current significantly affects the platform's CF motion, with a mitigated VIM and small CF motion being observed when the wave and current are colinear or having a small angle. Increasing the angle from 0° to 90° leads to a more significant VIM and larger CF motion, with the oscillation frequency being more synchronized with the system's natural

frequency. The motion displacement reaches its maximum at angle of 90°, where the motion induced by wave and current are in the same direction and coupled nonlinearly. A combination of largest wave height and the most significant VIM does not result in the largest CF motion. The motion can be even larger for smaller wave height, in some cases. The study of Keulegan–Carpenter number (*KC* numbers) and velocity ratio shows that the motion is mitigated if the problem is inertia-force dominant, whereas motion will be enhanced if it is drag-force dominated.

The interaction effect factor (*IEF*), which represents the motion ratio in wave–current condition compared to the sum motion in wave and current conditions separately, is evaluated. For large wave height and small wave period, the ratio is lower than 0.75, suggesting that the interaction of wave and current mitigates the sum of their individual motion. However, the most extreme motion does not necessarily take place with the largest wave height. With a smaller wave height, the ratio may be larger than 1.0. Remarkably, the interaction of wave and current could sometimes amplify the IEF to values as high as 1.35. At the design stage of floating offshore wind turbines platforms, these coupling effects have generally not been accounted for though it is sometimes critical as we illustrated. Therefore, our findings offer valuable insight for engineers considering the installation of wind turbines in regions where currents and waves coexist, potentially leading to more efficient and safer designs.

Although with the above findings, one limitation of the present study is the omission of wind loads and the resultant motion responses and critical elements in the interaction between FOWTs and current/waves. This is because the load generated by the upper turbine can alter the pitch and yaw motion, potentially influencing the vortex shedding around the structure. Although our current model does not include an aerodynamic simulation for wind turbines, future work is planned to expand the model's capabilities to address this aspect.

ACKNOWLEDGMENTS

AUTHOR DECLARATIONS
Conflict of Interest

The authors have no conflicts to disclose.

Author Contributions

Xiang Li: Conceptualization (equal); Investigation (equal); Methodology (equal); Validation (equal); Writing – original draft (equal); Writing – review & editing (equal). **Qing Xiao:** Conceptualization (equal); Methodology (equal); Project administration (equal); Resources (equal); Supervision (equal); Writing – original draft (equal); Writing – review & editing (equal). **Enhao Wang:** Conceptualization (supporting); Resources (supporting); Writing – review & editing (supporting). **Christophe Peyrard:** Conceptualization (supporting); Resources (supporting). **Rodolfo Trentin Gonçalves:** Conceptualization (supporting); Writing – review & editing (supporting).

DATA AVAILABILITY

The data that support the findings of this study are available within the article.

REFERENCES

[1]G. Stewart and M. Muskulus, "A review and comparison of floating offshore wind turbine model experiments," Energy Procedia **94**, 227 (2016).

[2]C. M. Wang, T. Utsunomiya, S. C. Wee, and Y. S. Choo, "Research on floating wind turbines: A literature survey," IES J. Part A: Civ. Struct. Eng. **3**, 267 (2010).

[3]M. A. Benitz, D. P. Schmidt, M. A. Lackner, G. M. Stewart, J. Jonkman, and A. Robertson, "Comparison of hydrodynamic load predictions between reduced order engineering models and computational fluid dynamics for the OC4-DeepCwind semi-submersible," in *Proceedings of 33rd International Conference on Ocean, Offshore and Arctic Engineering* (American Society of Mechanical Engineers, 2014), Paper No. OMAE2014-23985.

[4]H. Shin, *Model Test of the OC3-Hywind Floating Offshore Wind Turbine* (OnePetro, 2011).

[5]M. Borg, M. Walkusch Jensen, S. Urquhart, M. T. Andersen, J. B. Thomsen, and H. Stiesdal, "Technical definition of the TetraSpar demonstrator floating wind turbine foundation," Energies **13**, 4911 (2020).

[6]Y. Liu, Q. Xiao, A. Incecik, C. Peyrard, and D. Wan, "Establishing a fully coupled CFD analysis tool for floating offshore wind turbines," Renewable Energy **112**, 280 (2017).

[7]Y. Zhou, Q. Xiao, Y. Liu, A. Incecik, C. Peyrard, S. Li, and G. Pan, "Numerical modelling of dynamic responses of a floating offshore wind turbine subject to focused waves," Energies **12**, 3482 (2019).

[8]Y. Zhou, Q. Xiao, C. Peyrard, and G. Pan, "Assessing focused wave applicability on a coupled aero-hydro-mooring FOWT system using CFD approach," Ocean Eng. **240**, 109987 (2021).

[9]J. Chen, Z. Liu, Y. Song, Y. Peng, and J. Li, "Experimental study on dynamic responses of a spar-type floating offshore wind turbine," Renewable Energy **196**, 560 (2022).

[10]F. Duan, Z. Hu, and J. Niedzwecki, "Model test investigation of a spar floating wind turbine," Mar. Struct. **49**, 76 (2016).

[11]K. Kokubun, S. Ishida, T. Nimura, T. Chujo, S. Yoshida, and T. Utsunomiya, "Model experiment of a SPAR type offshore wind turbine in storm condition," in *Proceedings of 31st International Conference on Ocean, Offshore and Arctic Engineering* (American Society of Mechanical Engineers, 2012), Paper No. OMAE2012-83993.

[12]Q. Ding, C. Li, N. Yu, W. Hao, and J. Ji, "Numerical and experimental investigation into the dynamic response of a floating wind turbine spar array platform," J. Mech. Sci. Technol. **32**, 1106 (2018).

[13]A. J. Goupee, M. J. Fowler, R. W. Kimball, J. Helder, and E.-J. de Ridder, "Additional wind/wave basin testing of the DeepCwind semi-submersible with a performance-matched wind turbine," in *Proceedings of 33rd International Conference on Ocean, Offshore and Arctic Engineering* (American Society of Mechanical Engineers, 2014), Paper No. OMAE2014-24172.

[14]A. J. Goupee, B. Koo, K. Lambrakos, and R. Kimball, *Model Tests for Three Floating Wind Turbine Concepts* (OnePetro, 2012).

[15]T. Sarpkaya, "A critical review of the intrinsic nature of vortex-induced vibrations," J. Fluids Structs. **19**, 389 (2004).

[16]B. M. Sumer, *Hydrodynamics Around Cylindrical Strucures* (World Scientific, 2006).

[17]Y. Bao, C. Huang, D. Zhou, J. Tu, and Z. Han, "Two-degree-of-freedom flow-induced vibrations on isolated and tandem cylinders with varying natural frequency ratios," J. Fluids Struct. **35**, 50 (2012).

[18]R. T. Gonçalves, G. F. Rosetti, G. R. Franzini, J. R. Meneghini, and A. L. C. Fujarra, "Two-degree-of-freedom vortex-induced vibration of circular cylinders with very low aspect ratio and small mass ratio," J. Fluids Struct. **39**, 237 (2013).

[19]M. Zhao and L. Cheng, "Vortex-induced vibration of a circular cylinder of finite length," Phys. Fluids **26**, 015111 (2014).

[20]L. S. V. S. Sagrilo, M. Queija de Siqueira, T. A. N. Goncalves de Lacerda, G. B. Ellwanger, E. Castro Prates de Lima, and E. F. N. Siqueira, "VIM and wave-frequency fatigue damage analysis for SCRs connected to monocolumn platforms," in *Proceedings of 28th International Conference on Ocean, Offshore and Arctic Engineering* (American Society of Mechanical Engineers, 2009), Paper No. OMAE2009-79807.

[21]X. Liu, Z. Chen, Y. Si, P. Qian, H. Wu, L. Cui, and D. Zhang, "A review of tidal current energy resource assessment in China," Renewable Sustainable Energy Rev. **145**, 111012 (2021).

[22]M. Cueva, A. L. Fujarra, K. Nishimoto, L. S. Quadrante, and A. P. Costa, "Vortex-induced motion: Model testing of a monocolumn floater," in *Proceedings of 25th International Conference on Offshore Mechanics and Arctic Engineering* (American Society of Mechanical Engineers, 2006), Paper No. OMAE2006-92167.

[23]R. T. Gonçalves, A. L. Fujarra, G. F. Rosetti, and K. Nishimoto, "Mitigation of vortex-induced motion (VIM) on a monocolumn platform: Forces and movements," J. Offshore Mech. Arct. Eng. **132**, 041102 (2010).

[24]R. T. Gonçalves, G. F. Rosetti, A. L. Fujarra, and K. Nishimoto, "An overview of relevant aspects on VIM of spar and monocolumn platforms," J. Offshore Mech. Arct. Eng. **134**, 014501 (2012).

[25]R. T. Gonçalves, G. F. Rosetti, A. L. C. Fujarra, and A. C. Oliveira, "Experimental study on vortex-induced motions of a semi-submersible platform with four square columns, Part I: Effects of current incidence angle and hull appendages," Ocean Eng. **54**, 150 (2012).

[26]R. T. Gonçalves, M. E. F. Chame, L. S. P. Silva, A. Koop, S. Hirabayashi, and H. Suzuki, "Experimental flow-induced motions of a FOWT semi-submersible type (OC4 phase II floater)," J. Offshore Mech. Arct. Eng. **143**, 012004 (2021).

[27]Z. Du, X. Li, W. Xu, H. Zhu, J. Feng, W. Shen, and R. Jin, "An experimental investigation on vortex-induced motion (VIM) of a tension leg platform in irregular waves combined with a uniform flow," Appl. Ocean Res. **123**, 103185 (2022).

[28]A. L. Fujarra, F. Cenci, L. S. Silva, S. Hirabayashi, H. Suzuki, and R. T. Goncalves, "Effect of initial roll or pitch angles on the vortex-induced motions (VIM) of floating circular cylinders with a low aspect ratio," Ocean Eng. **257**, 111574 (2022).

[29]P. Jin, J. Liu, L. Xu, J. Wang, X. Ouyang, J.-H. Jiang, and J. Huang, "Tunable liquid–solid hybrid thermal metamaterials with a topology transition," Proc. Natl. Acad. Sci. U. S. A. **120**, e2217068120 (2023).

[30]Y. Liu, F. Liu, Q. Xiao, and L. Zhou, "The effect of inclination on vortex-induced vibration of a circular cylinder with a base column," Ocean Eng. **206**, 107332 (2020).

[31]Y. Liu, D. Ge, X. Bai, and L. Li, "A CFD study of vortex-induced motions of a semi-submersible floating offshore wind turbine," Energies **16**, 698 (2023).

[32]V. Vinayan, A. Antony, J. Halkyard, S.-J. Kim, S. Holmes, and D. Spernjak, "Vortex-induced motion of deep-draft semisubmersibles: A CFD-based parametric study," in *Proceedings of 34th International Conference on Ocean, Offshore and Arctic Engineering* (American Society of Mechanical Engineers, 2015), Paper No. OMAE2015-42209.

[33]H. Huang, H. Gu, and H.-C. Chen, "A new method to couple FEM mooring program with CFD to simulate six-DoF responses of a moored body," Ocean Eng. **250**, 110944 (2022).

[34]H. Huang and H.-C. Chen, "Investigation of mooring damping effects on vortex-induced motion of a deep draft semi-submersible by coupled CFD-FEM analysis," Ocean Eng. **210**, 107418 (2020).

[35]R. T. Gonçalves, L. A. Pinto, and A. L. C. Fujarra, "Experimental study on vortex-induced motions of a semi-submersible platform with four square columns, Part III: Effects of the collinear irregular and regular wave incidence and current," Ocean Eng. **217**, 107585 (2020).

[36]R. T. Gonçalves, G. F. Rosetti, A. L. C. Fujarra, and A. C. Oliveira, "Experimental study on vortex-induced motions of a semi-submersible platform with four square columns, Part II: Effects of surface waves, external damping and draft condition," Ocean Eng. **62**, 10 (2013).

[37]A. Maximiano, A. Koop, J. de Wilde, and R. T. Gonçalves, "Experimental study on the vortex-induced motions (VIM) of a semi-submersible floater in waves," in *Proceedings of 36th International Conference on Ocean, Offshore and Arctic Engineering* (American Society of Mechanical Engineers, 2017), Paper No. OMAE2017-61543.

[38]X. Li, Q. Xiao, R. T. Gonçalves, and C. Peyrard, "A coupled wave-current-structure study for a floating offshore wind turbine platform," in *Proceedings of 41st International Conference on Ocean, Offshore and Arctic Engineering* (American Society of Mechanical Engineers, 2022), Paper No. OMAE2022-79016.

[39]I. Bayati, M. Belloli, L. Bernini, E. Fiore, H. Giberti, and A. Zasso, *On the Functional Design of the DTU10 MW Wind Turbine Scale Model of LIFES50+ Project* (IOP Publishing, 2016).

[40]H. Jasak, A. Jemcov, and Z. Tukovic, *OpenFOAM: A C++ Library for Complex Physics Simulations* (IUC Dubrovnik, Croatia, 2007).

[41]F. Nicoud and F. Ducros, "Subgrid-scale stress modelling based on the square of the velocity gradient tensor," Flow, Turbul. Combust. **62**, 183 (1999).

[42]C. W. Hirt and B. D. Nichols, "Volume of fluid (VOF) method for the dynamics of free boundaries," J. Comput. Phys. **39**, 201 (1981).

[43]P. Higuera, "Enhancing active wave absorption in RANS models," Appl. Ocean Res. **94**, 102000 (2020).

[44]X. Li, Q. Xiao, Y. Zhou, D. Ning, A. Incecik, R. Nicoll, A. McDonald, and D. Campbell, "Coupled CFD-MBD numerical modeling of a mechanically coupled WEC array," Ocean Eng. **256**, 111541 (2022).

[45]Y. Liu, "A CFD study of fluid-structure interaction problems for floating offshore wind turbines," Ph.D. thesis (University Of Strathclyde, 2018).

[46]K. M. A. Kosasih, H. Niizato, S. Okubo, S. Mitani, and H. Suzuki, *Wave Tank Experiment and Coupled Simulation Analysis of Barge-Type Offshore Wind Turbine* (OnePetro, 2019).

[47]L. Wang, A. Robertson, J. Jonkman, J. Kim, Z.-R. Shen, A. Koop, A. Borràs Nadal, W. Shi, X. Zeng, E. Ransley, S. Brown, M. Hann, P. Chandramouli, A. Viré, L. Ramesh Reddy, X. Li, Q. Xiao, B. Méndez López, G. Campaña Alonso, S. Oh, H. Sarlak, S. Netzband, H. Jang, and K. Yu, "OC6 phase Ia: CFD simulations of the free-decay motion of the DeepCwind semisubmersible," Energies **15**, 389 (2022).

[48]Y. Liu, F. Liu, E. Wang, Q. Xiao, and L. Li, "The effect of base column on vortex-induced vibration of a circular cylinder with low aspect ratio," Ocean Eng. **196**, 106822 (2020).

[49]M. Saito, S. Masanobu, K. Taniguchi, K. Otsubo, T. Asanuma, and K. Maeda, "Experimental evaluation of VIM on MPSO in combined environmental conditions for waves and current," in *Proceedings of 31st International Conference on Ocean, Offshore and Arctic Engineering* (American Society of Mechanical Engineers, 2012), Paper No. OMAE2012-83283.

[50]T. Finnigan, M. Irani, and R. Van Dijk, "Truss Spar VIM in waves and currents," in *Proceedings of 24th International Conference on Offshore Mechanics and Arctic Engineering* (American Society of Mechanical Engineers, 2005), Paper No. OMAE2005-67054.

[51]T. Sarpkaya, "Force on a circular cylinder in viscous oscillatory flow at low Keulegan–Carpenter numbers," J. Fluid Mech. **165**, 61 (1986).

[52]M. Zhao, K. Kaja, Y. Xiang, and G. Yan, "Vortex-induced vibration (VIV) of a circular cylinder in combined steady and oscillatory flow," Ocean Eng. **73**, 83 (2013).

[53]Y. Iwagaki and T. Asano, "Hydrodynamic forces on a circular cylinder due to combined wave and current loading," Coastal Eng. Proc. **1**, 191 (1984).

[54]A. Robertson, J. Jonkman, M. Masciola, H. Song, A. Goupee, A. Coulling, and C. Luan, "Definition of the semisubmersible floating system for phase II of OC4," Technical Report No. NREL/TP-5000-60601, 2014.

16 February 2024 11:14:07